

Universität
Rostock



Traditio et Innovatio

Non-Hermitian topological photonics in coupled optical fibre loops

KUMULATIVE DISSERTATION

zur Erlangung des akademischen Grades
doctor rerum naturalium (Dr. rer. nat.)

vorgelegt dem Rat der Mathematisch-Naturwissenschaftlichen Fakultät
der Universität Rostock

von Sebastian Weidemann,
geboren am 10.12.1994 in Stralsund



Dieses Werk ist lizenziert unter einer
Creative Commons Namensnennung - Nicht kommerziell - Keine
Bearbeitungen 4.0 International Lizenz.

1. **Gutachter:** Prof. Dr. Alexander Szameit, Universität Rostock, Institut für Physik
2. **Gutachter:** Prof. Dr. Oded Zilberberg, Universität Konstanz, Fachbereich Physik
3. **Gutachter:** Prof. Dr. Hrvoje Buljan, Universität Zagreb, Fachbereich Physik

Jahr der Einreichung: 2022

Tag der Disputation: 10.03.2023

Zusammenfassung

In der vorliegenden Arbeit wird das Zusammenspiel zwischen Topologie, Unordnung und Dissipation sowohl theoretisch als auch experimentell untersucht. Eingebettet in das Feld der nicht-hermiteschen Physik werden eindimensionale Gittermodelle studiert, denen eine Schrödingergleichung mit nicht-hermiteschem Hamiltonian zugrunde liegt. Diese Modelle werden mittels der Ausbreitung von klassischen Lichtpulsen in gekoppelten Lichtleiterschleifen experimentell realisiert.

Zu Beginn wird der Einfluss stochastischer Dissipation auf die räumliche Ausbreitung der Ein-Teilchen-Wellenfunktion untersucht. Neben der resultierenden spektralen Lokalisierung wird eine neue und unerwartete räumliche Delokalisierung vorhergesagt und gemessen. Im Anschluss wird ein topologischer Trichtermechanismus für Licht vorgestellt und experimentell realisiert. Der Trichtermechanismus basiert auf nicht-hermitescher Topologie und aufgrund des topologischen Ursprungs ist der gewünschte Lichtfluss robust gegen Unordnung. Abschließend wird die Vorhersage und Beobachtung eines topologischen Dreifach-Phasenübergangs in einer Quasikristall-Gitterstruktur behandelt. Der beobachtete Dreifach-Phasenübergang betrifft die Topologie, die Lokalisierung der Energieeigenzustände und den Energieaustausch mit der Umgebung und offenbart einen potenziell engen Zusammenhang zwischen diesen zumeist als unabhängig erachteten Eigenschaften.

Abstract

In this thesis, the interplay between topology, disorder, and dissipation is investigated both theoretically and experimentally. Embedded into the field of non-Hermitian physics, one-dimensional lattice models are studied, which are governed by a Schrödinger equation with a non-Hermitian Hamiltonian. These models are experimentally implemented by means of classical light propagation in coupled optical fibre loops.

To begin with, the impact of stochastic dissipation on the spatial spreading of the single-particle wavefunction is studied. Besides the resulting spectral localization, a novel and unexpected spatial delocalization is predicted and measured. Afterwards, a topological funnelling mechanism for light is presented and experimentally realized. The funnelling mechanism is based on non-Hermitian topology and due to its topological origin, the desired flow of light is robust against disorder. This thesis is concluded with the prediction and observation of a topological triple phase transition in a photonic quasicrystal. The triple phase transition involves the topology, the energy eigenstate localization, and the energy exchange with the environment, indicating a potentially close relation between these properties, which are commonly viewed as independent.

Contents

1	Introduction	1
2	Fundamentals	3
2.1	Non-unitary quantum walks	3
2.2	Floquet-Bloch analysis	5
2.3	Topology	6
2.4	Experimental methods	8
2.4.1	Time-multiplexing	8
2.4.2	Experimental setup	10
3	Lattices under the influence of stochastic dissipation	13
3.1	Anderson localization	13
3.2	Localization in open quantum systems	14
3.3	Results	15
3.3.1	Mathematical description	15
3.3.2	Coexistence of dynamical delocalization and spectral localization . .	17
3.3.3	Photonic stochastic dissipation	18
3.3.4	Relation to current research and outlook	20
4	Topological funnelling of light	23
4.1	Breakdown of the bulk-boundary correspondence	23
4.2	Non-Hermitian topology	23
4.3	Results	24
4.3.1	Photonic coupling asymmetry	24
4.3.2	Topological analysis	26
4.3.3	Topological light funnelling	28
4.3.4	Robustness	29
4.3.5	Relation to current research and outlook	30
5	Non-Hermitian topological quasicrystals	31
5.1	PT symmetry	31
5.2	Phase transitions in quasicrystals	32
5.3	Results	32
5.3.1	Non-Hermitian photonic quasicrystals	33
5.3.2	Floquet Hofstadter butterfly	34
5.3.3	Topological triple phase transition	35
5.3.4	Relation to current research and outlook	38
6	Conclusion	39
	List of all publications	41
	Bibliography	41

1 Introduction

One of the fundamental axioms of quantum mechanics requires the Hamiltonian in the Schrödinger equation of a closed system to be a self-adjoint operator, which is typically represented by a Hermitian matrix. In contrast, in experiments one is always confronted with a system that is to some extent coupled to its environment. The presence of such dissipative processes is often considered a mere nuisance, whose theoretical treatment can be technically involved^[1].

This perception changed with the advent of non-Hermitian physics^[2–4], where the influence of the environment is captured by a non-unitary description of the considered subsystem, associated with effective Hamiltonians that are non-Hermitian^[5–7]. Under this approach, intriguing properties of open quantum systems with far-reaching physical consequences were identified, for instance, the occurrence of spectral singularities, so-called exceptional points in parameter space^[8–10], where two or more energy eigenvalues and their corresponding eigenvectors coalesce. An important milestone in the physics of non-Hermitian systems was the discovery by C.M. Bender and S. Boettcher^[11] that a large class of non-Hermitian Hamiltonians can exhibit entirely real spectra if they admit a combined parity-time (PT) symmetry, which can be understood as a non-Hermitian generalisation of quantum mechanics^[12]. Non-Hermitian descriptions proved fruitful for a plethora of physical settings^[2,4], but especially in optics and photonics^[10,13,14], where non-Hermitian systems, in particular ones with PT symmetry^[15], can be engineered in a controlled manner by judiciously incorporating optical gain and loss. As a result, deliberately shaping dissipation has become a rewarding approach for obtaining physical properties with promising applications, such as unidirectional invisibility^[16], exceptional-point-enhanced sensing^[17,18], or mode-selective laser cavities^[19,20].

The study of non-Hermitian systems is currently being further boosted due to its implications in the celebrated field of topological physics^[3,21]. Topology in physics relies on so-called topological invariants and their connection to observables^[22–24]. The quantized Hall conductivity, whose value is proportional to a topological invariant^[25], is arguably the most famous example for this relationship. Interest in topological physics surged further when new topological phases of matter were discovered, also known as quantum spin Hall systems or \mathbb{Z}_2 topological insulators, that do not break time-reversal symmetry, i.e., where external magnetic fields are not required. Since then, there have been intense efforts to understand which different topological phases of matter exist in the presence of various symmetries and in different dimensions, as well as to uncover what the ensuing physical consequences are^[26–29]. By identifying the essential ingredients for obtaining topological phases, numerous applications beyond the original realm of electronic systems have been found, for instance in photonic and microwave platforms^[30–34], mechanical and acoustic systems^[35,36], electric circuits^[37,38], ultracold atomic gases^[39,40] or based on ocean waves^[41]. The discovery of topologically protected phenomena, such as quantized response properties and scatter-free surface states, which are universal to a wide range of models, raises hopes that topological properties will facilitate new generations of devices, for instance in electronics and photonics, which potentially offer new functionalities while being more robust to imperfections. Inspired by the accomplishments of topological and non-Hermitian physics, there is currently an intense line of research on the combined field of non-Hermitian topological phases^[3,21,42], not least because of the vision that non-Hermiticity enriches the field of topology, as indicated by recent experiments reporting novel topological states in dissipative settings^[43–50].

The aim of this thesis is to investigate non-Hermitian topological phenomena for which fundamental open questions have not been theoretically or experimentally investigated yet. In order to validate the various theoretical findings of this thesis experimentally, discrete-time quantum walks are employed, because they may serve as a platform for a wide range of non-Hermitian^[16,51,52] and topological phenomena^[53-59] while their dynamics can be implemented efficiently via the propagation of light in coupled optical fibre loops, as done in this thesis.

In a first step, the theoretical foundations for the description of non-unitary quantum walks and their non-Hermitian Hamiltonians is provided, as well as their mapping onto the propagation of light in coupled optical fibre loops. The mathematical framework further covers basics of topology and Floquet theory, which lay the foundation for understanding the unique features of topological systems facilitated by temporally periodic parameters.

The next chapter is dedicated to the first publication of this thesis, [W1], in which the far-reaching physical consequences of stochastic dissipation, i.e., of random non-Hermitian contributions in the Hamiltonian, are investigated. The presence of dissipation with a certain degree of randomness should be relevant for a multitude of real systems. It is shown theoretically and experimentally that the interplay of randomness and dissipation leads to an unexpected breakdown of the correspondence between dynamical and spectral localization. This correspondence is a hallmark of Hermitian systems with uncorrelated disorder.

Based on the successfully established experimental control over the non-Hermiticity, in the next chapter, the anomalous relationship between bulk and boundary physics, arising in non-Hermitian systems, is studied. Being part of publication [W2], this involves a photonic implementation of so-called asymmetric (or non-reciprocal) coupling, which in turn allowed to realize the novel concept of topological light funnelling. The funnelling furthermore demonstrates the onset of the so-called non-Hermitian skin effect, hence implying the breakdown of the conventional (Hermitian) bulk-boundary correspondence. The observed topological states are explained by considering the topology of the complex energy spectrum, based on a non-Hermitian generalization of energy band gaps. Moreover, the topological states show robustness to a certain amount of disorder until a non-Hermitian delocalization-localization transition occurs, which is fully reflected in the experiments.

The following chapter is dedicated to publication [W3], which is the third and final one. Here, the non-Hermitian topology of a PT symmetric quasicrystals with asymmetric inter-site coupling is studied. Quasicrystals take on a special role in solid-state physics because they lack translational symmetry but still exhibit distinguished diffraction patterns. In the photonic quasicrystal, the interplay between aperiodic order, PT symmetry, and non-Hermitian topology induces a triple phase transition, which is predicted and measured. The term *triple* refers to the simultaneous occurrence of a topological phase transition, a PT phase transition and a delocalization-localization phase transition. Moreover, the photonic realization of aperiodic order gives rise to a Floquet version of Hofstadter's butterfly, which is observed within the Hermitian limit of the model.

The thesis ends with a conclusion, followed by a final chapter that contains the three publications with their corresponding supplementary information (SI).

2 Fundamentals

In this chapter, the theoretical and experimental foundation for the forthcoming chapters is presented. In a first step, the mathematical description of non-unitary quantum walks and their non-Hermitian Hamiltonians is outlined, followed by an analysis in the framework of Floquet-Bloch eigenstates. Afterwards, basic notions of topology in Hermitian and non-Hermitian systems are discussed. The chapter is concluded by an introduction to the experimental setup and an explanation on how the propagation of light pulses in coupled optical fibre loops can emulate non-unitary quantum walks.

2.1 Non-unitary quantum walks

Quantum walks can be viewed as quantum analogues of classical random walks^[60], which evolve either in continuous time^[61] or, as in this thesis, in discrete time steps^[62]. A discrete-time quantum walk is a succession of operators W acting on a quantum (walker) state $|\Psi\rangle \in \mathcal{H}$ of a Hilbert space \mathcal{H} such that the time evolution is determined by

$$|\Psi(m+1)\rangle = W |\Psi(m)\rangle, \quad (2.1)$$

proceeding in discrete time steps $m \in \mathbb{N}$, where $|\cdot\rangle$ refers to DIRAC's bra-ket notation^[63]. Within the scope of this thesis, the walker moves in a discrete one-dimensional space that is spanned by the basis states $\{|n\rangle\}_{n \in \mathbb{Z}} \in \ell^2(\mathbb{Z})$, describing the positional sites n . In addition, the walker features a spin-like *coin* degree of freedom at each positional site: The corresponding Hilbert space is spanned by the basis states $\{|L\rangle, |R\rangle\} \in \mathbb{C}^2$, which are represented by left- and right-going paths in the experimental implementation. From here on, the representation $|L\rangle = (1, 0)^\top$ and $|R\rangle = (0, 1)^\top$ is chosen.

The complete walker state therefore resides in the composite Hilbert space $\mathcal{H} = \ell^2(\mathbb{Z}) \otimes \mathbb{C}^2$ and it can be denoted as

$$|\Psi(m)\rangle = \sum_{n \in \mathbb{Z}} u_n^m |n\rangle \otimes |L\rangle + v_n^m |n\rangle \otimes |R\rangle, \quad (2.2)$$

with $u_n^m, v_n^m \in \mathbb{C}$ describing the corresponding probability amplitudes. The time-evolution operator W is built from a so-called coin-flip operator C , which is simply a transformation of the coin state, and a subsequent spatial shift operator S such that

$$W = SC, \quad (2.3)$$

with

$$C = \sum_{n \in \mathbb{Z}} |n\rangle \langle n| \otimes \tilde{C}_n, \quad S = \sum_{n \in \mathbb{Z}} \begin{pmatrix} |n-1\rangle \langle n| & 0 \\ 0 & |n+1\rangle \langle n| \end{pmatrix}, \quad (2.4)$$

and $\tilde{C}_n \in \mathbb{C}^{2 \times 2}$ being the local coin-flip at position n (Fig. 2.1). Within this thesis, \tilde{C}_n will have the general form

$$\tilde{C}_n = \begin{pmatrix} G_{u,n}^m e^{i\phi_{u,n}^m} & 0 \\ 0 & G_{v,n}^m e^{i\phi_{v,n}^m} \end{pmatrix} \begin{pmatrix} \cos(\beta_n^m) & i \sin(\beta_n^m) \\ i \sin(\beta_n^m) & \cos(\beta_n^m) \end{pmatrix}, \quad (2.5)$$

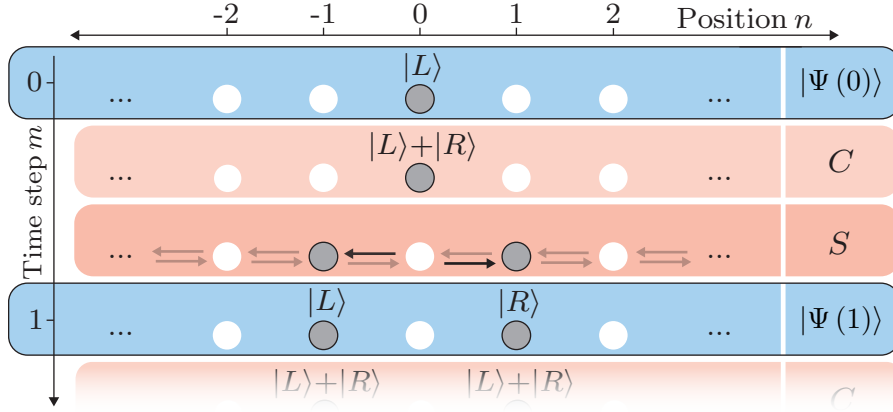


Figure 2.1 Quantum walk protocol: The action of the time-evolution operator $W = SC$ is visualized for a single time step starting with the initial state $|\Psi(0)\rangle = |0\rangle \otimes |L\rangle$. Applying the coin operator C changes the initial state to a superposition state comprising $|L\rangle$ and $|R\rangle$. Here, a simple unitary coin with symmetric coupling $\beta_n^m = \pi/4$ has been chosen in Eq. (2.5). Afterwards, the operator S shifts the $|L\rangle$ -state one site to the left and the $|R\rangle$ -state to the right, respectively. For the sake of simplicity, the values of u_n^m and v_n^m are not shown.

with the on-site terms $G_{i,n}^m \equiv G_i(m,n) \in \mathbb{R}_+$ and $\phi_{i,n}^m \equiv \phi_i(m,n) \in [0, 2\pi)$ for the internal state components $i \in \{u, v\}$, corresponding to an amplitude and phase modulation, respectively, and inter-site coupling coefficients $\beta_n^m \equiv \beta(m,n) \in [0, 2\pi)$.

The possibility of realizing non-unitary quantum walks W via the amplitude modulation $G_{u,v} \neq 1$ is at the heart of this thesis because it allows implementing non-Hermitian Hamiltonians^[2].

By additionally introducing temporal or spatial dependencies on the coin parameters in Eq. (2.5), a wide variety of physical phenomena can be emulated, as explained in the following chapters. For instance, breaking the spatial translation symmetry is one of the cornerstones of this thesis since it is generally necessary for observing topological states, or for implementing aperiodic or disordered structures. The use of temporally periodic modulations will become clear in the light of Floquet theory, as explained in the next section.

One can condense the time evolution of the quantum walk into the recursive equations

$$u_n^m = G_{u,n}^m (\cos(\beta_n^m) u_{n+1}^{m-1} + i \sin(\beta_n^m) v_{n+1}^{m-1}) e^{i\phi_{u,n}^m}, \quad (2.6)$$

$$v_n^m = G_{v,n}^m (i \sin(\beta_n^m) u_{n-1}^{m-1} + \cos(\beta_n^m) v_{n-1}^{m-1}) e^{i\phi_{v,n}^m}, \quad (2.7)$$

which can readily be used to determine the amplitudes u_n^m, v_n^m based on any initial distribution. From the perspective of quantum mechanics, the fields $|u_n^m|^2$ and $|v_n^m|^2$ may be understood as the probabilities to measure the walker at time step m and position n in the state $|L\rangle$ or $|R\rangle$, respectively, i.e., they result from the projective measurements

$$|u_n^m|^2 = |\langle n, L | \Psi(m) \rangle|^2, \quad |v_n^m|^2 = |\langle n, R | \Psi(m) \rangle|^2. \quad (2.8)$$

2.2 Floquet-Bloch analysis

The various evolution operators W discussed in this thesis exhibit periodic modulations in time step m in the form

$$W = \begin{cases} W_1, & m \text{ even,} \\ W_2, & m \text{ odd,} \end{cases} \quad (2.9)$$

and thus the time-evolution can be analysed by virtue of Floquet theory^[64]. The idea is that several concepts and methods used for time-independent systems can be carried over to time-periodic ones by describing the dynamics in the basis of the eigenstates of the Floquet operator, which is here $W_F \equiv W_2 W_1$. If the system additionally exhibits discrete spatial translation symmetry, one can obtain the corresponding eigenvalues and eigenstates by using a combined Floquet-Bloch ansatz^[16,65]

$$\begin{pmatrix} u_n^m \\ v_n^m \end{pmatrix} = \begin{pmatrix} U_{\theta,Q} \\ V_{\theta,Q} \end{pmatrix} e^{iQ\frac{n}{2}} e^{i\theta\frac{m}{2}}, \quad (2.10)$$

with the so-called quasienergy $\theta \in [-\pi, \pi)$ and quasimomentum $Q \in [-\pi, \pi)$. The factors 1/2 account for the size of the unit cell, which, without further modulations, covers two time steps and two positional sites (Fig. 2.2a). The ansatz can readily be adapted for larger unit cells. In a crystal, momentum becomes quasimomentum due to discrete spatial translational symmetry^[66], and energy likewise becomes quasienergy due to the discrete translation symmetry in time. Opposed to regular momentum and energy, θ and Q are periodic, as is clear from Eq. (2.10). By applying the Floquet-Bloch ansatz, one obtains the eigenvalue equation

$$W_F(Q) \begin{pmatrix} U_{\theta,Q} \\ V_{\theta,Q} \end{pmatrix} = e^{i\theta} \begin{pmatrix} U_{\theta,Q} \\ V_{\theta,Q} \end{pmatrix}, \quad (2.11)$$

where $W_F(Q)$ is in quasimomentum representation. Solving this eigenvalue problem yields the band structure $\theta = \theta_\nu(Q)$ as shown in Fig. 2.2b, with the band index ν labelling each quasienergy band. The energy bands give important insights about the dynamics, for instance the group velocity and dispersive broadening of wave packets, but also their reaction to external forces via the notion of an effective mass^[66]. Further, the existence of band gaps, i.e., ranges of energies not covered by any band, plays a paramount role in the band theory of insulators and is also a cornerstone of their topological classification^[55,67]. In systems without spatial translation symmetry, such as ones with aperiodic order as discussed in Chapter 5, the two-step temporal modulation still has a quasienergy spectrum associated with it though the conventional notion of a band structure is not valid anymore and hence the topological description must be modified.

A useful perspective for the theoretical description of these quantum walks opens up when formally associating the Floquet operator W_F with a stroboscopic simulation of a time-independent effective Hamiltonian H_F ^[56,57] via

$$W_F = e^{-iH_F \cdot \Delta T}, \quad (2.12)$$

where natural units are used here, i.e., $\hbar = 1$, and time is given in units of the driving period, i.e., the time which two steps of the quantum walk take, and hence $\Delta T = 1$. Based on Eq. (2.12), a time-periodic driving provides additional experimental dials to emulate static Hamiltonians, which might would have been inaccessible otherwise.

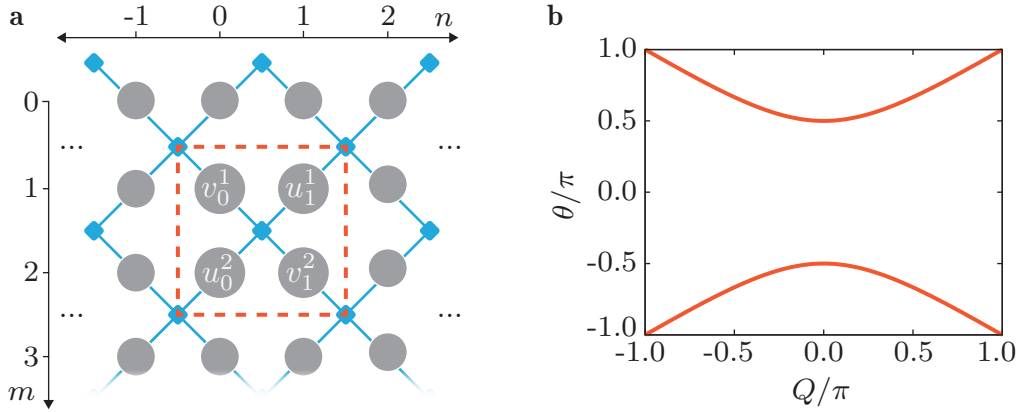


Figure 2.2 Floquet-Bloch quasienergy bands: **a**, As an example, a homogeneous lattice with symmetric coupling has been chosen, i.e., $G_{u,v} = 1$, $\phi_{u,v} = 0$ and $\beta = \pi/4$. In this case, the spatio-temporal unit cell (red dashed square) covers two time steps and two positional sites. The underlying graph structure (blue) features lattice sites (grey), which are connected by local coin-flip operations at the vertices. The site amplitudes u_n^m, v_n^m have been labelled within the unit cell. **b**, The corresponding quasienergy band structure is shown, which was obtained via the Floquet-Bloch ansatz, Eq.(2.10).

This approach has proven particularly fruitful for experimentally realizing non-trivial topological phases^[34]. Novel temporal driving protocols are likewise devised in this thesis. In passing, it should be noted that, in contrast to a truly static Hamiltonian, H_F has the previously discussed periodicity of quasienergy eigenvalues, which can potentially evoke (topological) features reserved to driven systems^[68–70].

In the case of a non-unitary time-evolution, H_F becomes non-Hermitian, i.e., $H_F^\dagger \neq H_F$. The \dagger symbol corresponds to the joint operation of transposition and complex conjugation. In contrast to the Hermitian case, the energy eigenvalues are generally complex, i.e., $\theta \in \mathbb{C}$. Moreover, H_F^\dagger and H_F do not necessarily share the same set of eigenstates anymore, and thus one must distinguish between left and right eigenstates^[4], which generally do not form an orthonormal set with the standard inner product. Within the scope of this thesis, in particular the occurrence of complex energy spectra will have a direct and far-reaching impact on the dynamics and gives rise to novel topological objects, as discussed in the following chapters.

2.3 Topology

The notion of band structures builds upon periodic and infinitely extended lattices, and hence it seems impractical for predicting the behaviour at boundaries, which naturally occur in real, and therefore finite-sized, systems. This perception changed with the advent of topology in physics^[25,26,71,72], which unveiled that bulk properties, i.e., properties of an infinite and periodic lattice, allow deriving edge properties. To do so, one relies on so-called topological invariants, which are quantized numbers, e.g., integers, that derive from the topological properties of the bulk. Topological properties can have different physical origins, and hence, there exist different topological invariants^[25,73–77], which, for instance, depend on the dimensionality of the system and the fulfilled or broken symmetries^[78], or whether the system is periodically driven^[68].

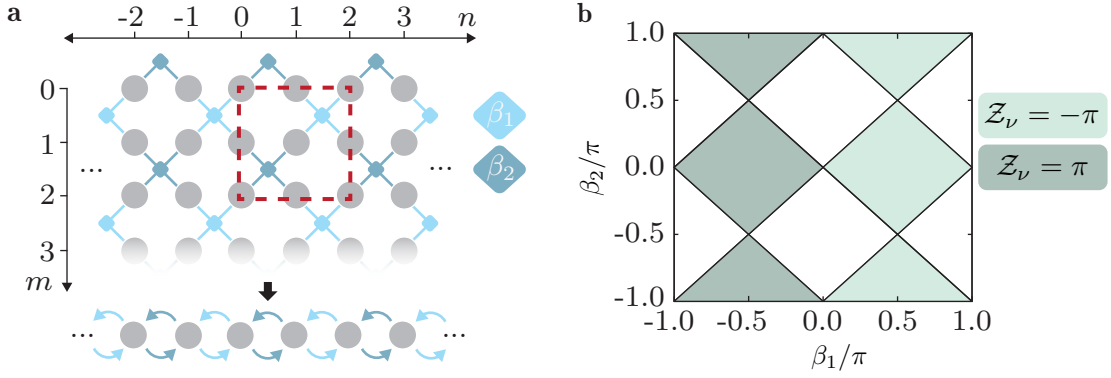


Figure 2.3 Quantum walk SSH model and its topology: **a**, The quantum walk implementation of the SSH model is shown. The green and blue boxes stand for different couplings β_1 and β_2 (top), giving rise to an effective Floquet SSH model (bottom). Grey filled circles represent the lattice sites. The unit cell is indicated by the red dashed square. **b**, The Zak phases of the Floquet SSH model are shown for different inter-site coupling parameters β_1 and β_2 . White areas correspond to vanishing Zak phases.

The topological invariants are related to physical observables, for instance through a so-called bulk-boundary correspondence^[23,53,79], which predicts the existence of topological boundary states if two bulk systems with different topological invariants are joined.

Due to their topological origin, these states are robust to a wide range of perturbations and therefore differ from ordinary bound states, which can appear whenever a system is perturbed locally. This robustness originates from the way a topological invariant is defined: Two systems have the same topological invariant, i.e., they are in the same topological phase, *if and only if* the underlying Hamiltonians are connected via continuous deformation while retaining certain key properties like an energy gap, crucial symmetries, and a locality condition^[67,79].

An archetypal example exhibiting non-trivial topological phases is the SU-SCHRIEFFER-HEEGER (SSH) model, which describes a 1D chain of nearest-neighbour coupled sites with two alternating couplings^[80]. A Floquet implementation of the SSH model can be realized via quantum walks^[56–58,81], and it is also part of this thesis in Chapter 4. The corresponding two-step Floquet operator reads

$$W_F = SC(\beta_1)SC(\beta_2), \quad (2.13)$$

where $C(\beta_i)$ follows from Eq. (2.5) with $\tilde{C} = \exp(i\beta_i\sigma_x)$ with σ_x denoting the first Pauli matrix. The model has no additional gain-loss or phase modulation, i.e., $G_{u,v} = 1$ and $\phi_{u,v} = 0$. The two-step modulation effectively translates to a linear chain of sites with two alternating couplings, β_1 and β_2 , as shown in Fig. 2.3a.

According to the topological classification of one-dimensional systems^[55,67], a suitable invariant for this Hermitian system is the so-called *Zak phase*^[75], which is defined as

$$\mathcal{Z}_\nu = i \int_{-\pi}^{\pi} \psi_\nu^\dagger \frac{\partial}{\partial Q} \psi_\nu dQ, \quad (2.14)$$

where ψ_ν denote the non-degenerate eigenstates of $H_F = i \log W_F$ in the quasienergy band ν . The Zak phases of the Floquet SSH model can be calculated to be either 0 or $\pm\pi$ ^[79,82], as displayed in the phase diagram in Fig. 2.3b. At the interface between two subsystems with different Zak phases a topological interface state emerges^[23,53,79]. The topological description of non-Hermitian systems is discussed in Chapter 4 and 5.

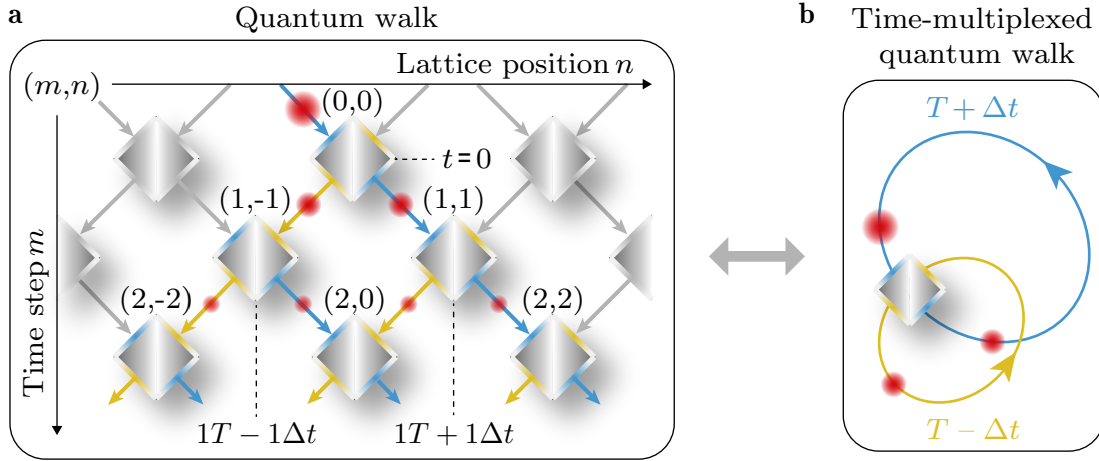


Figure 2.4 Time-multiplexed photonic quantum walks: **a**, The propagation of a light pulse (red-filled circle) in a mesh lattice of beam splitters resembles a photonic quantum walk. **b**, The propagation of light in coupled optical fibre loops yields the same quantum walk, but requires much less components, because it is temporally encoded. Here, the initial pulse splits up into two pulses, which return to the splitter with a time difference of $2\Delta t$. This delay corresponds to an arrival at two separated splitters as shown on the right. The resulting interplay of temporal delays and multipath interference forms the time-multiplexed quantum walk. The time step m corresponds to the number of roundtrips and the positional site n is shifted due to relative delays; $+1$ for taking the long loop and -1 for taking the short loop.

2.4 Experimental methods

2.4.1 Time-multiplexing

The tremendous technological advances of the last decades have facilitated the observation of quantum walks in a multitude of experimental settings, for instance, based on nuclear magnetic resonances^[83,84], trapped ions^[85,86], atoms^[87,88], or photonic systems^[89–93].

The experiments in this thesis rely on a photonic implementation that utilises time as an external degree of freedom^[16,54,58,94,95]. The discussed quantum walks could in principle be realized by the propagation of light in a network of optical beam splitters (Fig. 2.4a), which can be understood by the following three observations:

First, left and right going paths represent the internal coin degree of freedom $|L\rangle$ and $|R\rangle$. Second, each beam splitter is labelled by a tuple (m, n) where different time steps m and positions n correspond to different rows and columns, respectively. Each beam splitter contributes to the local coin-flip operation $\tilde{C}(m, n)$ in Eq. (2.5) via the splitting parameter β_n^m and the additional amplitude and phase modulation. Third, the optical connections to neighbouring beam splitters hence realize the desired spatial shifts induced by the operator S .

However, based on this scheme, large lattices are experimentally infeasible due to the huge amount of components involved. To overcome this problem, an alternative implementation is used, which still yields the same dynamics. By employing the so-called method of time-multiplexing^[96], only two loops of optical fibre are required, which are coupled by a single beam splitter as visualized in Fig. 2.4b.

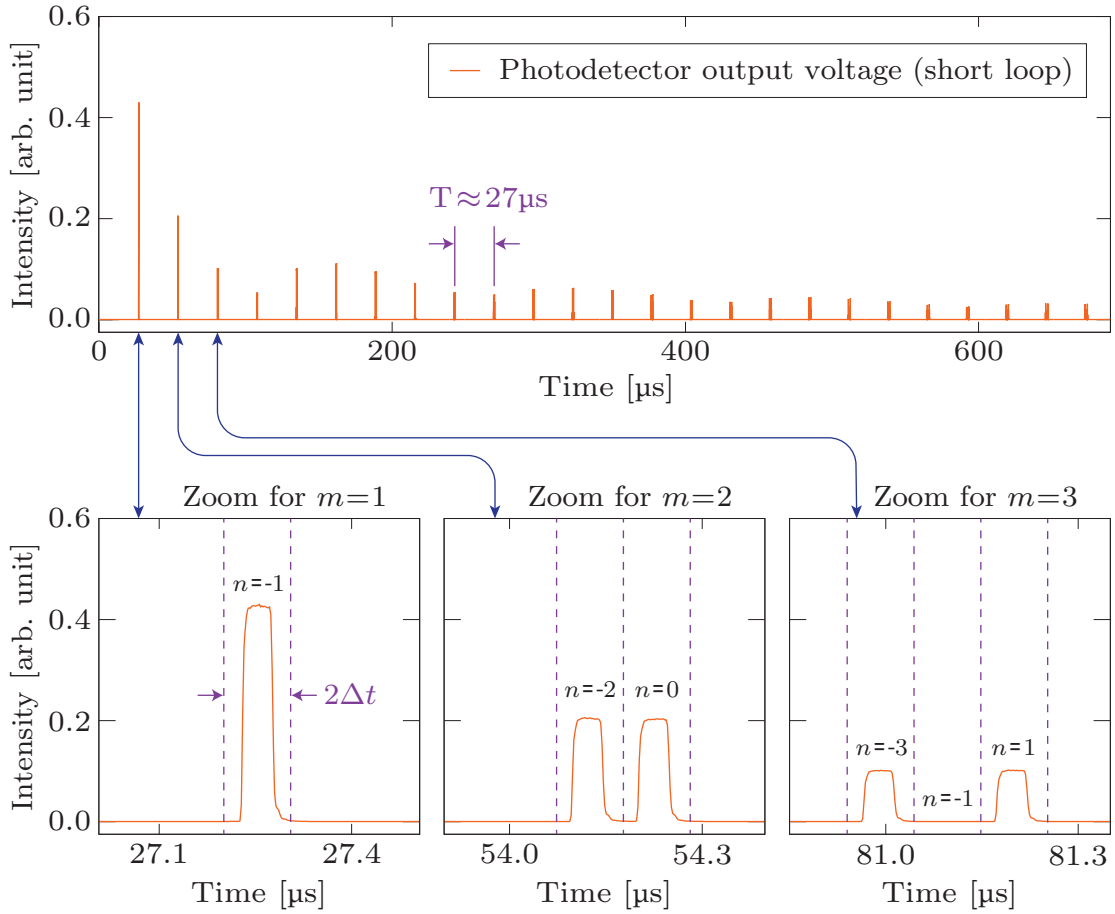


Figure 2.5 Mapping of time-multiplexed data: The time-resolved photodetector output voltage is shown for the first 25 roundtrips upon sending a single pulse into the longer loop. The output voltages correspond to the light intensities in the short loop. By averaging over the pulse plateau in individual time-bins n in roundtrip m , one obtains $|u_n^m|^2$ from Eq. (2.7), up to a normalization given by the arbitrary unit, as later shown in Fig. 2.7. The beam splitter was set to equal splitting, $\beta_n^m = \pi/4$, and no further modulations were applied. A small fraction of the light was continuously coupled out to a photodetector and optical losses were counterbalanced via amplification as explained in the following. For the sake of simplicity, only data from the short loop is shown.

The time-multiplexing works as follows: Upon launching a light pulse into the optical network and subsequently measuring the coin and position state after m roundtrips in the loops, the distributions $|u_n^m|^2$ and $|v_n^m|^2$ are obtained^[96]. Measuring light in the short or long loop determines the coin state, corresponding to the projective measurements in Eq. (2.8). Here, each roundtrip maps onto a time step m , and taking the longer or shorter loop additionally leads to a shift in position space n to the left or right, respectively, i.e., the position is encoded in relative time delays $n \cdot \Delta t$ (see Fig. 2.5).

The time-multiplexing thus allows for an unambiguous assignment of a time step m and position n to each pulse based on its overall propagation time $mT + n\Delta t$ if the following two conditions are fulfilled: First, the used pulse duration must be smaller than the time-bin of a position state, Δt , and second, the accumulated difference in delays between pulses must not exceed the roundtrip time T . It follows that a time-resolved intensity measurement in both optical fibre loops suffices to fully reconstruct $|u_n^m|^2$ and $|v_n^m|^2$.

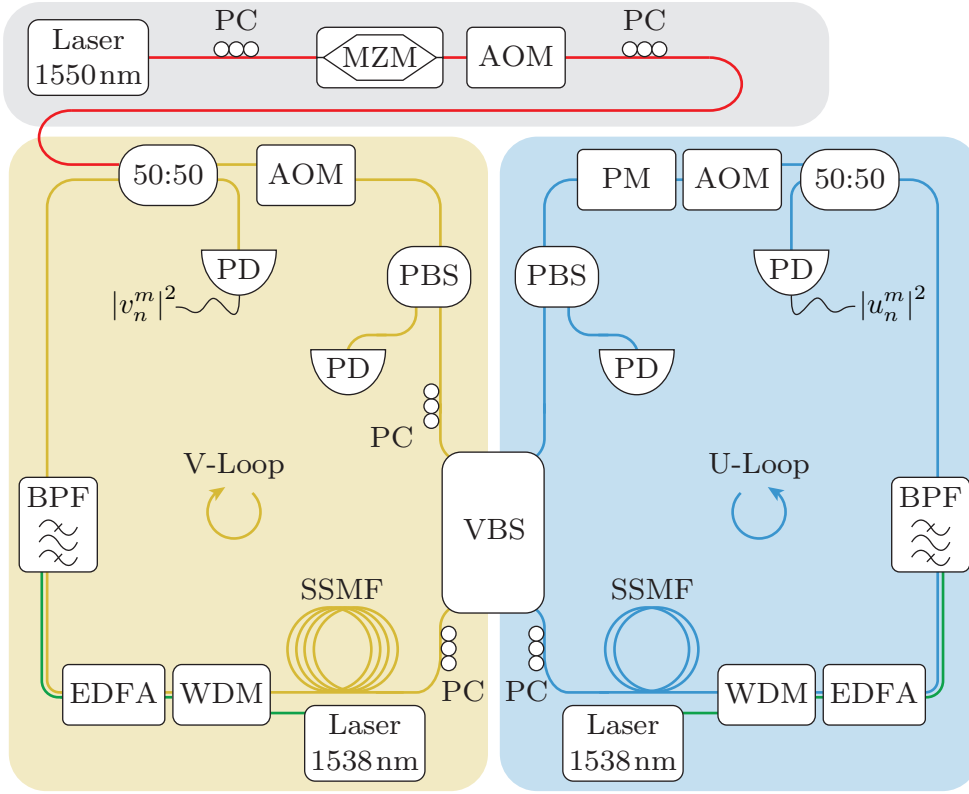


Figure 2.6 Experimental setup: The optical setup consists of the signal generation (grey) and the longer optical fibre loop (yellow), which is coupled to the shorter loop (blue). The operating principle and all abbreviations are explained in this section.

2.4.2 Experimental setup

The employed experimental setup is based on previous works^[16,59,94], and, within the scope of this thesis, it has been systematically extended to access regimes that had been out of reach before. The extended setup allows to change the coupling between the optical fibre loops dynamically, as explained below. Moreover, an unprecedented control over optical gain and loss is achieved while maintaining a high signal-to-noise ratio. These features form the basis for realizing the topological interfaces and the non-Hermitian models presented in this thesis.

The setup can be divided into three building blocks, which are marked by differently coloured areas in Fig. 2.6. The grey area marks the pulse generation. Here a continuous wave distributed-feedback laser is employed together with an external intensity modulation via a Mach-Zehnder modulator (MZM) and an acousto-optic modulator (AOM). The intensity modulators form a rectangular-shaped 50 ns pulse, which is then coupled into the loop arrangement. This marks the beginning of the quantum walk and for its duration no other light is injected.

The yellow area contains the loop with the roundtrip time $T + \Delta t$, while the blue area contains the shorter loop with roundtrip time $T - \Delta t$. The longer loop is dubbed v-loop because it contains exclusively the pulse intensities $|v_n^m|^2$ and, analogously, the shorter loop is called u-loop.

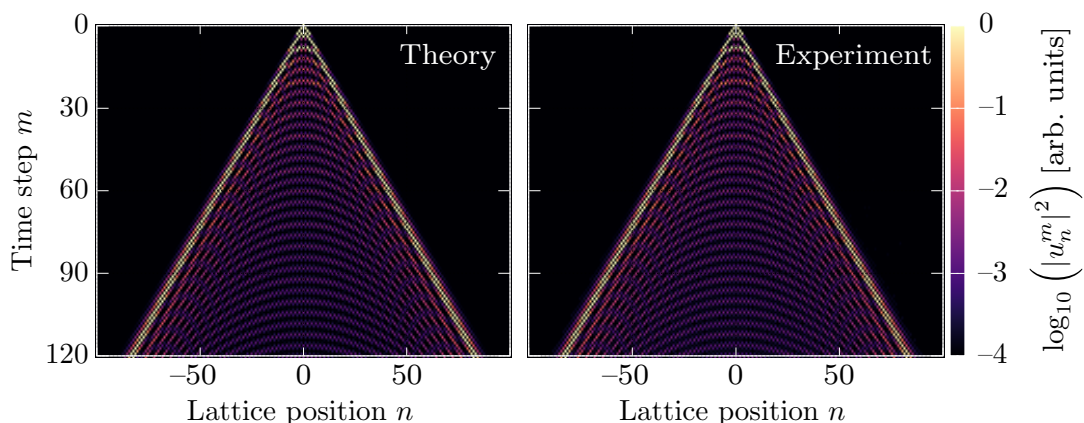


Figure 2.7 Experimental test: Theory (left) and measured pulse intensities (right) in the shorter loop for over 120 roundtrips, which have been mapped on the (1+1)D lattice. The result corresponds to $|u_n^m|^2$ from Eq. (2.7) up to a normalization to the maximum value each roundtrip, which is given by the arbitrary unit. The beam splitter was set to equal splitting, $\beta_n^m = \pi/4$, and no further modulations were applied. The experiment started by sending a single pulse into the longer loop, i.e., $v_n^0 = \delta_{n,0}$. For the sake of simplicity, only the data from the short loop is shown. Experimental data from publication [W1].

Light is exchanged between the loops via a variable beam splitter (VBS), whose coupling ratio determines β_n^m in Eq. (2.5). As an example, switching between two different splitting ratios every other roundtrip corresponds to the modulation in the Floquet SSH model in Eq. (2.13). Additional beam splitters couple 50% of the light to photodetectors (PD) that measure the pulse intensities in each roundtrip.

Spools of standard single mode fibre (SSMF) provide an overall roundtrip time of $T \approx 27 \mu\text{s}$. The difference in propagation time between the loops is $2\Delta t \approx 100 \text{ ns}$. Erbium-doped fibre amplifiers compensate the optical roundtrip losses, which also includes the light coupled out for detection. The amplifiers are optically gain-clamped via an external laser signal, which is added to the loops via wavelength-division multiplexing (WDM) couplers. Bandpass filters (BPF) remove the gain-clamping signal and reduce optical noise induced by the amplification process.

To modulate the phase and amplitude of the propagating pulses, further AOMs and a phase modulator (PM) are employed, which determine $G_{u,n}^m$, $G_{v,n}^m$ and $\phi_{u,n}^m$ in Eq. (2.5), respectively. Note, that no phase modulation is required in the v-loop, because in the discussed projects only the relative phase differences between interfering amplitudes matter. The operating point of the AOMs is set to 50% transmission so that increasing or decreasing the transmission will lead to an effective gain or loss, respectively. The 0th diffraction order is aligned to the AOM outputs in order to achieve amplitude modulation without frequency shifts. A polarization beam splitter (PBS) and polarization controllers (PC) are used to monitor and align the optical polarization. This alignment is required in front of polarization-sensitive components like the MZM and the PM. Moreover, both loops have to provide pulses with the same polarization state when combining them at the VBS because otherwise the interference contrast decreases.

Arbitrary waveform generators drive the electro-optic devices and all lattice parameters are determined by the designed electronic waveforms. The signals from the photodetectors are amplified with logarithmic voltage amplifiers and afterwards sampled with an oscilloscope. The acquired data is then mapped onto $|u_n^m|^2$ and $|v_n^m|^2$ (Fig. 2.7).

3 Lattices under the influence of stochastic dissipation

In this chapter, the impact of stochastic dissipation on single-particle wave dynamics in one-dimensional lattices is investigated. The mathematical description relies on the analysis of the eigenstates and complex energy spectra of Hamiltonians with randomized non-Hermitian contributions, i.e., non-Hermitian disorder. The theoretical predictions are applied to non-unitary photonic quantum walks and experimentally verified. Before turning to the results of the corresponding publication [W1], this chapter starts with an introduction to the phenomenon of Anderson localization, describing the impact of disorder in Hermitian settings, followed by a summary of the current research on its non-Hermitian extensions, which naturally leads to the case of stochastic dissipation discussed here.

3.1 Anderson localization

With the advent of quantum mechanics, physicists could finally understand why electrons apparently do not scatter from ions that occupy regular lattice sites: Owing to their wave characteristics, electrons diffract from the ideal crystal^[97] and electrical resistance appears due to scattering from crystal imperfections. However, in 1958, Philip Anderson made the intriguing discovery that beyond a critical amount of such lattice disorder, conductivity is not just reduced, but instead the previously metallic material can abruptly turn into an insulator^[98]. The underlying spatial localization of the single-particle electron wavefunction, also known as *Anderson localization*, is based on elementary wave interference between multiple-scattering paths and therefore applies not only to electrons in solids^[99,100], but also to electromagnetic waves^[101–103], matter waves^[104,105] and sound waves^[106], for instance. Anderson’s groundbreaking discovery revolutionized the understanding of disordered media and after stimulating decades of studies^[107], Anderson localization has found applications in various areas of physics^[108–116].

Anderson localization has also been predicted for discrete-time quantum walks^[117–119] and was observed in time-multiplexed, photonic settings^[120,121]. Here, the on-site disorder of the original tight-binding model^[98] can be introduced by treating the on-site terms $\phi_{u,n}^m \in [-W, W]$ in Eq. (2.5) for each site n as independent random variables, which are drawn from the same uniform probability distribution, i.e., the disorder is spatially uncorrelated. The maximal applied phase shift W is a measure of the disorder strength.

For non-zero disorder strength, all eigenstates of H_F become exponentially localized in space, which is a hallmark of Anderson localization, also dubbed *spectral localization*^[122,123]. Their inverse localization lengths may be calculated from^[124]

$$L_{\text{loc}}^{-1}(\theta) = - \lim_{N \rightarrow \infty} \frac{1}{N} \log \left(\frac{|\psi_\theta(N)|}{|\psi_\theta(1)|} \right), \quad (3.1)$$

with $\psi_\theta(n)$ denoting the Floquet eigenstates of H_F with quasienergy eigenvalue θ . Here, $N \rightarrow \infty$ describes the so-called thermodynamic limit for the lattice with sites $n = 1 \dots N$, and $|\psi_\theta(1)| \neq 0$ is used for the amplitude normalization. The exponential localization of all eigenstates can therefore be described by finding finite localization lengths $L_{\text{loc}} < \infty$ for all energies.

Concomitant to the spectral localization is the so-called *dynamical localization*^[122], which implies that for any spatially localized wave packet all orders $\nu \in \mathbb{N}$ of the statistical moment M_ν of its position operator, i.e.,

$$M_\nu(m) = \mathbb{E} \left[\sum_{n \in \mathbb{N}} \left(|n|^\nu \frac{|u_n^m|^2 + |v_n^m|^2}{\sum_{k \in \mathbb{N}} (|u_k^m|^2 + |v_k^m|^2)} \right) \right], \quad (3.2)$$

are uniformly bounded in time m . In the following, the expectation value $\mathbb{E}[\cdot]$ is approximated by averaging over many random realizations of the disorder. The numerator corresponds to the probability of finding a particle with wavefunction $|\Psi(m)\rangle$ at position n , in accordance with Eq.(2.8). The denominator corresponds to a normalization, which can differ from the value 1 only in non-Hermitian settings, as the ones discussed in this thesis. The moments M_ν are related to the wave packet displacement from its origin $n = 0$, and hence, dynamical localization is a strong form of describing the absence of diffusion.

A hallmark of the theory of Anderson localization in Hermitian systems with uncorrelated disorder is the equivalence between spectral localization and dynamical localization: On one hand, independently of disorder correlations, dynamical localization implies spectral localization, as concluded from the RUELLE–AMREIN–GEORGESCU–ENSS (RAGE) theorem^[122,125], which relates the long-time behaviour of solutions of the Schrödinger equation to the spectral properties of the corresponding self-adjoint Hamiltonian (see references for a detailed discussion). On the other hand, under rather weak conditions^[126], which are always satisfied for uncorrelated disorder^[123], spectral localization implies dynamical localization^[122,123]. Only in special cases of correlated disorder, for instance as in the random dimer model^[127], wave spreading might still occur in the presence of spectral localization^[126].

3.2 Localization in open quantum systems

Anderson’s theory relies on Hermitian Hamiltonians, i.e., it naturally assumes the conservation of energy and particle number within the system, even though real systems inevitably exchange both with their environments. Since the phenomenon of Anderson localization relies on long-range interference, one might intuitively expect that dissipation simply impairs or destroys the localization. However, the interplay between disorder and dissipation gives rise to much richer physics. A seminal example for this is Mott’s model of hopping conductivity for disordered solids at low temperatures, where a phonon-assisted hopping between the localized charge-carrier states facilitates the conductivity^[128,129].

Recently, new light was shed on this subject by a number of works considering disordered settings in which dissipation gives rise to new and unexpected phenomena^[130–140], for instance, a tunable localization of states^[138] or the appearance of so called ‘Anderson attractors’^[130,134]. Being a result of Chapter 4, the onset of dissipation in 1D disordered systems can even induce a delocalization transition^[132,133]. Moreover, systems with bulk dissipation or with open boundaries were considered, showing that dissipation can impair weak localization and open boundaries can lead to a position-dependent diffusion, where the diffusion coefficient drops significantly as the position changes from the boundary to the bulk^[137,141–143]. In such settings, the interplay of dissipation and localization can also facilitate anomalous transmission via so-called necklace states^[140], i.e., highly transmitting superpositions of overlapping localized eigenstates^[144,145].

In most of the previous works, the impact of adding dissipation to a disordered medium was considered. However, studies in which the dissipation is not merely an addition, but instead the source of the disorder, remain almost elusive. On the contrary, the case of dissipation with a certain degree of randomness should be applicable to a variety of real systems. Wave transport in structures with random absorption is for example found in ultrasound and optical imaging techniques, especially those concerned with human tissue. Considering a non-Hermitian Hamiltonian, the case of stochastic dissipation can be obtained by transferring the random changes of the on-site terms in the original Anderson model from the real to its imaginary part. Against all intuition, recent studies predicted that such settings can also exhibit spectral localization as in the original model^[131,135].

A direct experimental observation of this non-Hermitian spectral localization requires the implementation of tunable stochastic dissipation in many large samples in which either the spectrum or the time-evolution can be measured. Because of the implied technical challenges, any experimental observations remained elusive so far.

In addition, it is still an open question whether the predicted non-Hermitian spectral localization, induced by stochastic dissipation, also implies dynamical localization like in the Hermitian case. The complex and stochastic nature of the energy eigenvalues in systems with stochastic dissipation potentially breaks the correspondence, as explained and observed in the following results.

3.3 Results

In this section, the results of publication [W1] are presented. This involves the first experimental observation of spectral localization induced by stochastic dissipation. In a first step, a theory is developed, which predicts the onset of wave spreading in systems with static, uncorrelated dissipation that is randomly distributed in a 1D space. This dynamical delocalization is experimentally observed although the same experiments indicate that all eigenstates are exponentially localized. The results imply the breakdown of the correspondence between spectral and dynamical localization known from the Hermitian Anderson model. Against all intuition, the stochastic dissipation is not only the origin of the spectral localization, but it simultaneously causes the observed dynamical delocalization. Moreover, within the scope of this thesis, the achieved experimental control over the disorder and non-Hermitian contributions paves the road for the experiments on non-Hermitian topological systems presented in the Chapter 4 and 5.

3.3.1 Mathematical description

In open quantum systems, the question arises of how transport or wave spreading may be distinguished since the probability of finding the particle within the considered subspace is not a conserved quantity anymore. While it is still possible to define an energy or probability flux, it remains challenging to disentangle transport within the subsystem from mere dissipation. For example, whereas in conservative systems dynamical delocalization necessarily implies a continuous flow of energy or probability, this is not necessarily the case for non-conservative systems, where delocalization can arise from a spatially non-uniform distribution of eigenstate lifetimes, as discussed below. Another counter-intuitive effect underlining the complexity of transport in open systems is the existence of an energy flow among the occupied sites of localized eigenstates, even though their spatial distribution does not change in time^[146,147].

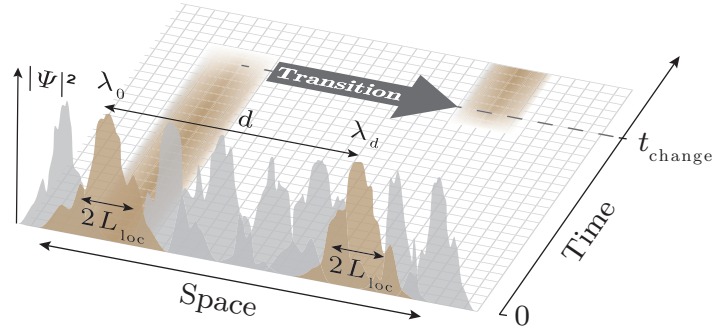


Figure 3.1 Dynamical delocalization in lattices with stochastic dissipation: The exponentially localized eigenstates are subject to dynamic population changes, which are described by the presented theoretical model. As a starting point, one assumes that initially an eigenstate with the decay rate $\text{Im}(\lambda_0)$ is dominant. Another eigenstate localized at distance d and with decay rate $\text{Im}(\lambda_d) > \text{Im}(\lambda_0)$ becomes dominant after the time t_{change} , which depends on the overlap between the states, i.e., on their localization lengths L_{loc} and the distance d . Figure adapted from publication [W1].

In all following considerations, the position of an observer who has no a priori knowledge about the initial state and dissipation is taken. This corresponds to the protocol applied in single-photon experiments in the field of non-Hermitian photonics^[48,148,149], where non-detection events, for instance caused by dissipated photons, are not part of the statistics. This post-selection can be expressed by a normalization of the total probability as introduced in the denominator of Eq. (3.2). Consequently, changes of the population of the eigenstates, which occur exclusively in non-Hermitian systems, potentially lead to dynamical delocalization even when all eigenstates are exponentially localized.

The following theory for the wave dynamics in systems with stochastic dissipation is based on a time-independent 1D Hamiltonian whose on-site terms have randomized imaginary parts. The discussed case of spatially uncorrelated disorder is achieved by treating the dissipation for each site n as independent random variables that pertain to the same probability distribution. To begin with, a single-site excitation is considered. Further, it is assumed that all eigenstates are exponentially localized. This assumption is supported by recent theoretical works^[131,135] and it will also be shown in the following experiments. The population of the eigenstates is determined by the spatial overlap with the excitation. The corresponding weight factors are proportional to $\exp(-d/L_{\text{loc}})$, where d is the distance between the states and L_{loc} the localization length of the localized state. Let ψ_j denote an exponentially localized eigenstate with energy eigenvalue λ_j . The weight factor belonging to eigenstate j is modified by a decay term $\exp(\text{Im}(\lambda_j)t)$ with an imaginary part $\text{Im}(\lambda_j) < 0$ due to the dissipation. As a result of different decay rates, the relative population of the eigenstates changes over time. For simplicity, it is assumed that at $t = 0$ mainly the eigenstate with eigenvalue λ_0 is excited. In the thermodynamic limit there is almost surely another state with a smaller decay rate $\text{Im}(\lambda_d) > \text{Im}(\lambda_0)$. Due to the resulting change in population, this eigenstate will become dominant at a time t_{change} , which is determined by

$$\text{Im}(\lambda_d) t_{\text{change}} - \frac{d}{L_{\text{loc}}} = \text{Im}(\lambda_0) t_{\text{change}}. \quad (3.3)$$

At this point, the dominantly occupied eigenstate has changed from the excited state to the one at distance d , as shown in Fig. 3.1. This line of reasoning implies the breakdown of dynamical localization in spite of the spectral localization. To quantify the dynamical delocalization, one can calculate the moments in Eq. (3.2) via

$$M_\nu(t) = \sum_{n \in \mathbb{Z}} |n|^\nu P_n(t), \quad (3.4)$$

where $P_n(t)$ denotes the probability that the population maximum changes from site $n = 0$ to n after the time t . The decay rates $\text{Im}(\lambda_j)$ follow a random distribution $f(\rho)$ ^[131] and the probability for a transition of the population maximum to a state with a decay rate in the range $(\rho, \rho + d\rho)$ is determined by the joint probabilities that all other states $j \neq n$ are not dominant at time t , i.e.,

$$\text{Im}(\lambda_j)t - \frac{|j|}{L_{\text{loc}}} < \rho t - \frac{|n|}{L_{\text{loc}}}. \quad (3.5)$$

The transition probability can therefore be calculated by

$$P_n(t) = \int_{\frac{|n|}{L_{\text{loc}}}}^{\infty} d\rho f(\rho) \prod_{j \neq n} \int_{-\infty}^{\rho + \frac{|j| - |n|}{L_{\text{loc}}}} d\rho f(\rho). \quad (3.6)$$

The product of the inner integrals gives the probability that all other states $j \neq n$ have a decay rate smaller than ρ . The outer integral presents the probability that the state at distance $|n|$ has an eigenvalue ρ large enough to observe the transition at time t . This derivation requires that the decay rates $\text{Im}(\lambda_j)$ are independent stochastic variables that belong to the same distribution $f(\rho)$. This assumption is particularly valid as long as the eigenstates extend only over a few sites, which is the case for strong uncorrelated disorder^[131]. Further, it is assumed that almost all eigenstates have the same localization length L_{loc} .

Importantly, only few assumptions were used for the derivation of Eq. (3.6), and it should therefore be applicable to a multitude of settings. In this vein, it is demonstrated in the next sections that the developed theory applies well to the case of photonic discrete-time quantum walks, where instead of a continuous time variable t , the evolution proceeds in discrete time steps m .

3.3.2 Coexistence of dynamical delocalization and spectral localization

To efficiently capture the dynamical delocalization in one single quantity, the wave spreading coefficient

$$s = \lim_{t \rightarrow \infty} \frac{d \log M_2(t)}{d \log t}, \quad (3.7)$$

is defined. It is a common measure for the wave spreading and based on the asymptotic behaviour of the second spatial moment. For comparison, ballistic spreading is characterized by a coefficient of $s = 2$, whereas $s = 1$ describes diffusive spreading^[149]. In contrast, dynamical localization is characterized by a vanishing spreading coefficient $s = 0$.

The case of stochastic dissipation is realized by treating the amplitude modulations $G_{u,n}^m$ and $G_{v,n}^m$ in Eq. (2.5) as independent random variables for each site n . For the experiments, the dissipation distribution

$$G_{u,n}^m = G_{v,n}^m = e^\gamma, \quad \gamma \in [-W, W], \quad (3.8)$$

is used, which is uniform in the on-site decay (growth) rates γ . This distribution also includes optical gain $\gamma > 0$ because it allows maintaining a high signal-to-noise ratio in the experiments compared to a purely passive system. However, mathematically the presented results do not depend on whether a purely passive system or a system with gain and loss is chosen^[131], because in the framework of classical wave propagation these systems can be connected by a suitable gauge transformation, for instance represented by a global (n independent) gain or loss term in each time step. A similar analogy is also used in non-classical settings where systems with gain and loss can be emulated by purely passive systems^[148,150,151].

For a sufficiently large disorder strength W , all eigenstates extend over single sites only, and in this case one can analytically derive the probability distribution of the decay rates

$$f(\rho) = \begin{cases} \frac{2W+\rho}{4W^2}, & -2W \leq \rho \leq 0 \\ \frac{2W-\rho}{4W^2} & 0 < \rho \leq 2W \\ 0 & |\rho| > 2W \end{cases}, \quad (3.9)$$

which is a triangular distribution bounded by the minimal and maximal possible decay or growth rate that can occur after two time steps, i.e., $-2W$ and $2W$, respectively. Two time steps must be considered when solving the eigenvalue problem, because of the temporal periodicity of the lattice, as explained in Section 2.2. When using the rescaled decay rate $\tilde{\rho} = \rho W/2$ and time $\tilde{t} = tW L_{\text{loc}}/2$, the probabilities in Eq. (3.6) take the form

$$P_n(\tilde{t}) = \begin{cases} 0, & |n| > \tilde{t} \\ \int_{\frac{|n|}{\tilde{t}}}^1 d\tilde{\rho} (1 - \tilde{\rho}) \prod_{j \neq n}^{|j| < (1-\tilde{\rho})\tilde{t} + |n|} \left(1 - \frac{1}{2} \left(1 - \tilde{\rho} - \frac{|j|-|n|}{\tilde{t}} \right)^2 \right), & |n| < \tilde{t}. \end{cases} \quad (3.10)$$

This important result allows to derive the spreading coefficient s based on Eq. (3.4) and Eq. (3.7) without knowledge of the localization length L_{loc} and the disorder strength W . One obtains $s \rightarrow 4/3$, which agrees perfectly with the results obtained from the numerical time-evolution of single-site excitations in the case of strong disorder $W > 2$ (see SI of [W1]). Hence, the first objective, i.e., the prediction of the coexistence of spectral localization and dynamical delocalization, is therefore achieved. In the next step, this result is experimentally tested.

3.3.3 Photonic stochastic dissipation

To study the dynamics in disordered lattices experimentally, the light propagation in coupled optical fibre loops is employed, as introduced in Chapter 2. For comparison, the dynamics in two lattice types are monitored upon exciting a single site: First, a lattice with Hermitian disorder, resembling the original Anderson model, and second, a lattice with stochastic dissipation. The underlying quantum walk models and measured wave dynamics are shown in Fig. 3.2. For the sake of simplicity, only the optical intensity distribution $|u_n^m|^2$ is used from the experimental data because differences to the other fibre loop are only on a local scale and vanish upon averaging, which was confirmed numerically.

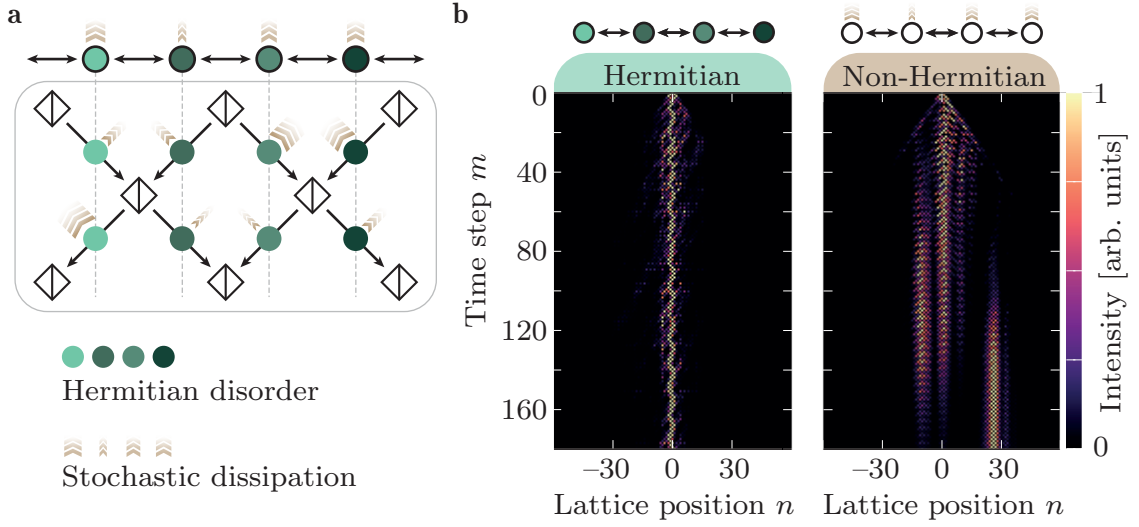


Figure 3.2 Experimental light propagation in disordered lattices: **a**, Two quantum walk models of disordered (1+1)D lattices are shown. Different shades of green correspond to different real on-site terms $\phi_{u,n}^m$, resembling the disorder of the original Anderson model. Different arrow widths correspond to different dissipation strengths realized via the amplitude modulation Eq. (3.8), which resembles the stochastic dissipation. The two disorder types are not applied simultaneously. All models employ symmetrical coupling $\beta_n^m = \pi/4$. **b**, The experimental data, $|u_n^m|^2$, shows Anderson localization in the case of Hermitian disorder (left, $W = 0.7\pi$). In contrast, the propagation in lattices with stochastic dissipation (right, $W = 0.19$) indicates localized eigenstates whose population changes dynamically, leading to dynamical delocalization. Figure adapted from publication [W1].

The lattice resembling the Hermitian Anderson model is realized by random changes in the real part of the on-site terms. This is implemented by choosing $\phi_{u,n}^m \in [-W, W]$ with $W = 0.7\pi$ for each site n as independent random variables that pertain to the same uniform distribution, whereas $G_{u,n}^m = G_{v,n}^m = 1$. In agreement with previous works^[120,121], all spatial wave transport comes to complete halt, indicating that all eigenstates are exponentially localized (Fig. 3.2). This is in sharp contrast to the propagation in a homogeneous lattice without disorder, i.e., $G_{u,n}^m = G_{v,n}^m = 1$, $\phi_{u,n}^m = 0$, yielding ballistic spreading^[149] with all eigenstates extended (see Fig. 2.7 in Chapter 2).

The case of stochastic dissipation is realized by randomly distributing on-site gain and loss as described by Eq. (3.8), with disorder strength $W = 0.19$. Importantly, no Hermitian disorder is required, i.e., $\phi_{u,n}^m = 0$. The experimental results in Fig. 3.2 show that a single-site excitation localizes, which is in agreement with the predicted spectral localization^[131]. Nevertheless, transverse shifts of the dominantly occupied eigenstates are observed as predicted by the developed theoretical model. The displayed wave propagation differs drastically from the Hermitian case since it indicates dynamical delocalization despite spectral localization. To further corroborate the coexistence of spectral localization and dynamical delocalization, 40 lattices with different random realizations of stochastic dissipation are realized. To evaluate the exponential localization of eigenstates, the resulting 40 intensity distributions $|u_n^m|^2$ are averaged at a large time step to approximate the long-time behaviour. Before averaging, they are spatially shifted to share the same centre to avoid the ambiguity of the positions of the populated eigenstates. The result in Fig. 3.3a shows the exponential localization by a linear decay in the logarithmic scale.

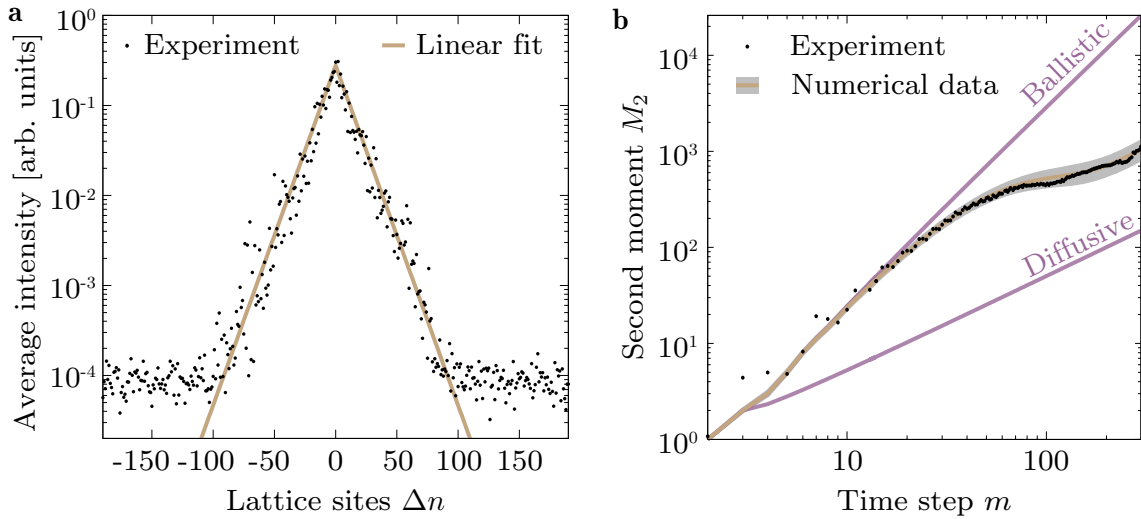


Figure 3.3 Coexistence of spectral localization and dynamical delocalization through stochastic dissipation: **a**, Centred intensity distribution $|u_n^m|^2$ at time step $m = 110$ and averaged over 40 lattices with different random realizations of dissipation. The disorder strength is fixed at $W = 0.19$. The experimental data displays exponential localization. **b**, Time evolution of the second moment $M_2(m)$, based on the same 40 realizations. For a much larger number of disorder realizations, the numerical data converges to the shown line for stochastic dissipation. The grey area displays ± 1 s.d. of expected statistical fluctuations arising from using only 40 disorder realizations. Figure adapted from publication [W1].

To evaluate the dynamical delocalization, the second spatial moment $M_2(m)$ is calculated based on the acquired wave propagation in the 40 different lattices. The experimental data shows dynamical delocalization comparable to a super-diffusive system as predicted by the theory and despite the fact that the same data indicated that all eigenstates are localized (Fig. 3.3b). Hence, the theoretically predicted breakdown of the correspondence between spectral and dynamical localization is fully reflected in the experiments. A remarkable result of the theory and experiments is that the stochastic dissipation is not only the source of the spectral localization, but it simultaneously facilitates the dynamical delocalization. The presented results raise questions about whether the dynamical delocalization, induced by stochastic dissipation, prevails in lattices where the real parts of the potential are also randomized. The developed theory implies that the stochastic dissipation would still facilitate the dynamic changes in the eigenstate population that can lead to dynamical delocalization. This is indeed observed in additional experiments that were performed within the scope of this thesis (see SI of [W1]).

3.3.4 Relation to current research and outlook

In the original Anderson model, localization depends on the dimensionality of the considered space. In Hermitian 1D and 2D systems, Anderson localization occurs for arbitrary disorder strengths $W > 0$, whereas in 3D there exists a non-zero threshold at which the metal-insulator transition occurs. The presented results might suggest that lattices with stochastic dissipation also exhibit thresholdless spectral localization in 1D and recent theoretical studies indicate the same in 2D^[135]. However, the non-Hermitian system discussed in the next chapter shows Anderson localization with a threshold, even though the un-

derlying space is 1D, and this is expected to apply also to the case of non-Hermitian disorder^[21]. Moreover, Anderson localization with non-Hermitian disorder is also studied in 3D systems^[136,152], suggesting the existence of a localization transition similar to the Hermitian case.

Future works could investigate a theoretical framework for also describing the regime of weak disorder, i.e., where the assumptions of the developed theoretical model are potentially invalid. Here, one would need to take into account the substantial overlap of the eigenstates, which could then also capture the transition to the ballistic spreading of a disorder-free lattice.

Beyond being in the interest of fundamental physics, the results potentially contribute to turning stochastic dissipation into use, for instance when designing disordered (photonic) materials with tailored optical properties and functionalities^[102]. Extending the studies into the realm of correlated disorder could facilitate new opportunities for creating materials that strongly scatter and absorb (or amplify) light at specific wavelengths or angular distributions [W4]. Since the developed theoretical model is based on a general eigenstate and eigenvalue analysis, the presented results can be applied in principle to numerous platforms beyond photonics, such as matter waves, acoustic waves, and electrons.

4 Topological funnelling of light

In this chapter, the extreme sensitivity of the eigenvalue spectrum of certain non-Hermitian Hamiltonians to their boundary conditions is utilized to realize the novel concept of topological light funnelling. In addition, its topological robustness against disorder is tested. The corresponding topological description needs to incorporate non-Hermiticity and it drastically differs from its Hermitian counterpart. Before turning to the results of publication [W2], the chapter starts with an introduction to the so-called non-Hermitian skin effect, which describes their topological basis.

4.1 Breakdown of the bulk-boundary correspondence

When studying periodic systems, the approximation of an infinitely expanded setting is frequently used, even though it is never fulfilled in any experiment. However, when compared to the infinite setting, notable differences in the eigenstates and energy eigenvalues are expected to occur only locally, i.e., close to boundaries. Consequently, the approximation of an infinitely expanded setting can be justified if the system under investigation is large enough. A prominent example for this is the topological boundary mode in the Hermitian SSH model, which can appear at the boundary between two regions with different Zak phases, as introduced in Section 2.3. Besides the appearance of this mode, the eigenmode spectrum of the bulk does essentially not change when introducing a boundary.

Recent works^[42,153–156] show that this common wisdom can fail in non-Hermitian systems, where an asymmetric (non-reciprocal) inter-site coupling, i.e., $|h_{ij}| \neq |h_{ji}|$ is the source of the non-Hermiticity in the matrix representation of the Hamiltonian, $H_F = (h_{ij})$ ^[21]. In such systems, changing from periodic boundary conditions to open boundary conditions can cause a dramatically non-perturbative localization of all bulk modes at the boundary. This phenomenon is dubbed *non-Hermitian skin effect*^[42] as it appears phenomenologically similar to the skin effect known from electrodynamics, though with regard to their physical origin the two effects are distinct. The prediction of the non-Hermitian skin effect questions the validity of the bulk-boundary correspondence in non-Hermitian systems^[42,153–155,157,158] because the extreme sensitivity of bulk spectra to the boundaries renders the notion of coexisting bulk and boundary properties invalid. However, despite the extreme spectral sensitivity, the non-Hermitian skin effect has a topological origin^[21,159], and it is expected to be a topologically robust and generically observable phenomenon^[160].

4.2 Non-Hermitian topology

Novel and topologically stable phenomena originate from non-Hermiticity, for instance, the non-Hermitian skin effect^[3,161]. These phenomena are related to two main observations that occur in the topological description of non-Hermitian systems: First, the energy spectrum is generally complex, and hence the notion of energy band gaps must be adapted^[3,21,162]. It turns out that non-Hermitian systems host two complementary types of energy gaps, point gaps^[21] and line gaps^[3], and both are associated with different physical phenomena. The spectrum is defined to have a point (line) gap if and only if its complex-energy bands do not cross a reference point (line), as shown later in Fig. 4.3.

Second, one has to distinguish between left and right eigenstates, which are in general not orthogonal. As a consequence, approaches relying on biorthogonal quantum mechanics are employed to construct a bulk-boundary correspondence that remains valid for non-Hermitian systems with a line gap^[158]. In this context, it is emphasized that not all non-Hermitian systems exhibit the breakdown of the conventional bulk-boundary correspondence^[3,21]. This was, for example, shown in experimental works^[46,48,163,164], demonstrating that for dissipative systems with broken or unbroken PT symmetry^[165] it is possible to derive topological invariants from the Bloch Hamiltonian that correctly predict the existence of topological states.

A fruitful approach to account for these observations is to take into account the full complex eigenvalue spectrum when deriving topological invariants^[21]. This drastically differs from the Hermitian case, where the topology is instead encoded in the geometrical properties of the eigenstates but not in the shape of the energy spectrum^[67]. In particular for the non-Hermitian topological systems studied in this thesis, the employed topological invariant is the winding of the energy eigenvalues in the complex plane

$$w = \frac{1}{2\pi i} \int_{-\pi}^{+\pi} dk \partial_k \log \det (H(k) - \mathbb{1}E_B), \quad (4.1)$$

for an invertible Bloch Hamiltonian, i.e., $\det H(k) \neq 0$, with k denoting the Bloch momentum. The non-Hermitian topological objects which are characterized by a non-zero spectral winding number are closed loops in the complex energy plane that encircle a base energy $E_B \in \mathbb{C}$. The corresponding topological phases are distinguished by different integer values of the winding number and a transition between two distinct phases requires a crossing of the base energy. The existence of such a base energy resembles a non-Hermitian extension of the Hermitian band gap, i.e., the point gap mentioned above^[3]. The topology of the non-Hermitian skin effect is described by a point gap and it was predicted that, like in the Hermitian case, systems with non-zero winding numbers can host topological boundary states^[21].

4.3 Results

In this section, the results of the publication [W2] are presented. This involves the first experimental observation of the non-Hermitian skin effect in a photonic system and its utilization for topological light funnelling. The topological funnelling is the observation that any light field within the lattice, irrespective of its input position and spatial distribution, travels toward a narrow funnelling region, which is represented by a topologically non-trivial interface. To observe the non-Hermitian skin effect, a photonic implementation of asymmetric coupling is developed. Moreover, being a hallmark of topological effects, the robustness of the funnelling mechanism against disorder is tested.

4.3.1 Photonic coupling asymmetry

In the following, the two models shown in Fig. 4.1 are compared. The first model is the SSH model, which is a chain of nearest-neighbour coupled lattice sites with alternating coupling constants, as introduced in Section 2.3. The second model also features an alternating coupling, however, it is non-Hermitian because every other coupling is asymmetric in the sense that the hopping from one site to its neighbour differs from the hopping from its neighbour back to itself.

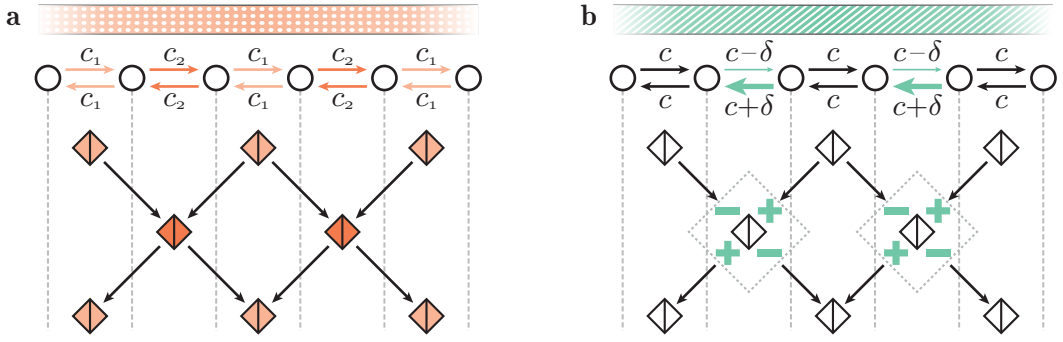


Figure 4.1 SSH model vs. non-Hermitian skin effect model: **a**, The SSH model consists of a linear chain of nearest-neighbour coupled sites with alternating coupling strengths c_1 and c_2 . This Hermitian model with isotropic coupling is indicated by the dotted orange ribbon. The mapping to the Floquet photonic lattice is shown below. Different shades of orange represent different beam splitting ratios (coupling strengths), as discussed in Section 2.3. **b**, The non-Hermitian skin effect model consists of a linear chain of nearest-neighbour coupled sites with asymmetric coupling every other site, i.e., coupling strengths $c + \delta$ in the left direction and $c - \delta$ in the right direction. In contrast to the SSH model, the beam splitting ratio is not modulated. This asymmetric modulation is indicated by the ribbon with angled green stripes. Due to the amplitude modulation given by Eq. (4.6), the beam splitters in every second row can be translated to their asymmetric counterpart, as indicated by green plus and minus signs that represent the gain-loss modulation. Figure adapted from the publication [W2].

As shown later in this section, such asymmetric coupling can facilitate the non-Hermitian skin effect on the basis of which the topological light funnelling will be demonstrated. In this vein, in a first step an experimental scheme for implementing the coupling asymmetry in a photonic setup is devised.

To do so, one starts with a minimal setup of two sites with asymmetric coupling. The Hamiltonian of this setting has the form

$$H = \begin{pmatrix} 0 & -c - \delta \\ -c + \delta & 0 \end{pmatrix}, \quad (4.2)$$

and yields the time evolution matrix

$$\exp(-iHt) = \begin{pmatrix} \cos(t\sqrt{c^2 - \delta^2}) & \frac{i(c+\delta)}{\sqrt{c^2 - \delta^2}} \sin(t\sqrt{c^2 - \delta^2}) \\ \frac{i\sqrt{c^2 - \delta^2}}{(c+\delta)} \sin(t\sqrt{c^2 - \delta^2}) & \cos(t\sqrt{c^2 - \delta^2}) \end{pmatrix}. \quad (4.3)$$

This matrix can be written as

$$\exp(-iHt) = \begin{pmatrix} e^{\rho/2} & 0 \\ 0 & e^{-\rho/2} \end{pmatrix} \begin{pmatrix} \cos \beta & i \sin \beta \\ i \sin \beta & \cos \beta \end{pmatrix} \begin{pmatrix} e^{-\rho/2} & 0 \\ 0 & e^{\rho/2} \end{pmatrix}, \quad (4.4)$$

with

$$\beta = \sqrt{c^2 - \delta^2}, \quad \exp(\rho) = \frac{c + \delta}{\sqrt{c^2 - \delta^2}}. \quad (4.5)$$

This corresponds to a beam splitter operation with an additional amplification-attenuation modulation before and after the splitting process.

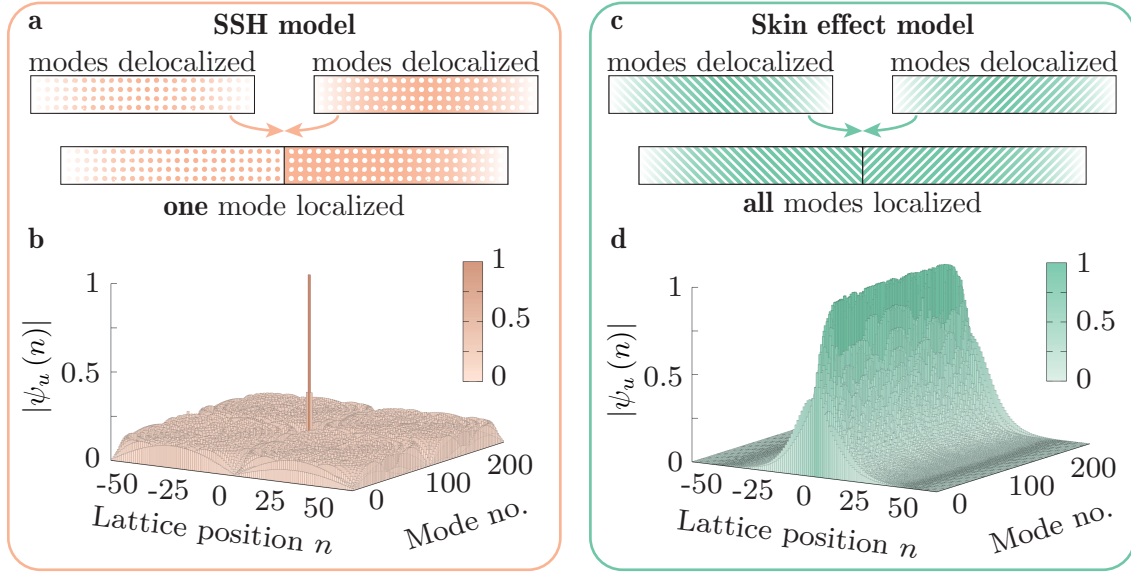


Figure 4.2 Eigenstates in the presence of an interface: **a**, Two SSH lattices are interfaced. The inverted ribbon indicates the inverted coupling ratio, yielding different topological phases at either side, as discussed in Section 2.3. **b**, The corresponding eigenmodes $\psi_u(n)$ pertaining to u_n^m are shown for a lattice with 120 lattice sites. **c**, Two lattices with asymmetric coupling are interfaced. The inverted ribbon indicates the inverted coupling asymmetry $\delta \rightarrow -\delta$, yielding different non-Hermitian topological phases, as discussed below. **d**, The corresponding eigenmodes are plotted for a lattice with 120 lattice sites. For the numerical calculation of the eigenmodes, periodic boundary conditions were used. Figure adapted from the publication [W2].

Based on the coupled optical fibre loops, a photonic mesh lattice of those active beam splitters is realized, as explained in Chapter 2 and visualized in Fig. 4.1. It should be noted that by using a fibre-optical beam splitter in the experiments, the outputs are interchanged compared to free-space optical beam splitter cubes^[166]. The gain-loss modulation after the beam splitter needs to be changed accordingly, and hence, one loop is always experiencing amplification, while the other one is always experiencing attenuation. The resulting gain-loss modulation in Eq. (2.5) for the photonic coupling asymmetry reads

$$G_{u,n}^m = (G_{v,n}^m)^{-1} = \exp\left(\frac{\rho}{2}\right), \quad (4.6)$$

while $\phi_{u,n}^m = \phi_{v,n}^m = 0$. Interestingly, such a modulation also arose in the context of PT-symmetric Bloch oscillations^[52]. For the following theory and experiments, an amplification and attenuation strength of $\rho = 0.33$ is used.

4.3.2 Topological analysis

A topologically non-trivial interface can be introduced in the SSH lattice by inverting the ratio c_1/c_2 for all sites after some position, as illustrated in Fig. 4.2a, where the inverted ribbon indicates the inverted coupling ratio. As a result, a single state localizes at the interface, which is well known as a topological mode^[80]. All other states, however, remain delocalized, which is in agreement with the common perception that in a Hermitian system the bulk spectrum remains essentially unchanged.

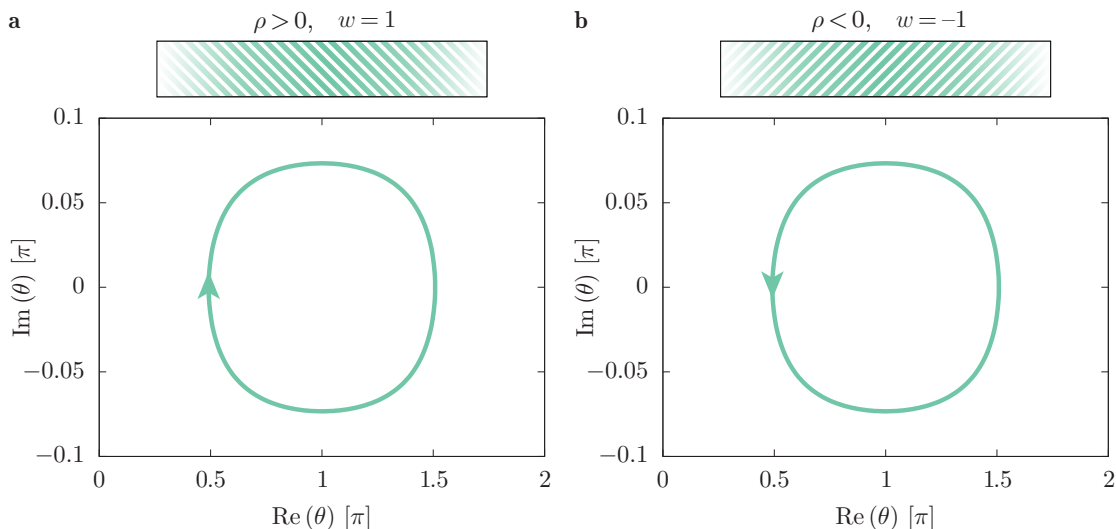


Figure 4.3 Topological invariant of the skin effect model: The quasienergy spectra and the corresponding winding numbers, Eq. (4.7), are shown for the two different modulations $\pm\rho$, corresponding to the two ribbons with differently angled stripes. The winding direction for $Q \in (-\pi, \pi)$ is indicated by the arrows. Note that the bands in Eq. (4.8) are already merged as the winding number takes into account the sum of the two bands, $\theta = \theta_+ + \theta_-$. Figure adapted from publication [W2].

The outcome is completely different when introducing an interface in the non-Hermitian lattice with asymmetric coupling. A topologically non-trivial interface is created by reversing the direction of the coupling asymmetry at some position (Fig. 4.2c). As a result, all eigenstates become exponentially localized at the interface (Fig. 4.2d), turning all former bulk states into boundary states, which is exactly the non-Hermitian skin effect. In sharp contrast to the Hermitian case, even far away from the interface the spectrum is greatly affected, indicating the breakdown of the conventional bulk-boundary correspondence. This behaviour can be related to the topological properties of the underlying lattice as follows: Based on the introduced topological invariant in Eq. (4.1), one can define a winding number for the skin effect quantum walk model, which reads

$$w = \sum_{\nu=1}^N \frac{1}{2\pi} \int_{-\pi}^{\pi} dQ \arg(\theta_{\nu}(Q) - \theta_B), \quad (4.7)$$

where N is the total number of bands and $\theta_{\nu}(Q)$ are the corresponding quasienergies in each band. The encircled base energy is denoted by $\theta_B = \pm\pi$ and describes the spectral degeneracy due to the underlying Floquet nature of the system. Upon using the Floquet-Bloch ansatz, Eq. (2.10), one obtains the two complex energy bands

$$\theta_{\pm}(Q) = \pm \arccos(\cos(Q - i\rho) \cos^2 \beta - \sin^2 \beta), \quad (4.8)$$

whereas in the following the balanced beam splitting parameter $\beta_n^m = \beta = \pi/4$ is chosen. The resulting spectral winding is shown in Fig. 4.3. One can see that the direction of the coupling asymmetry determines the direction of the spectral winding. The two sides of the non-Hermitian interface therefore possess different winding numbers, giving rise to a continuum of topological interface states^[21].

The non-Hermitian eigenstate collapse has profound implications for the dynamics: A topological funnelling of waves is facilitated, as shown in the next section.

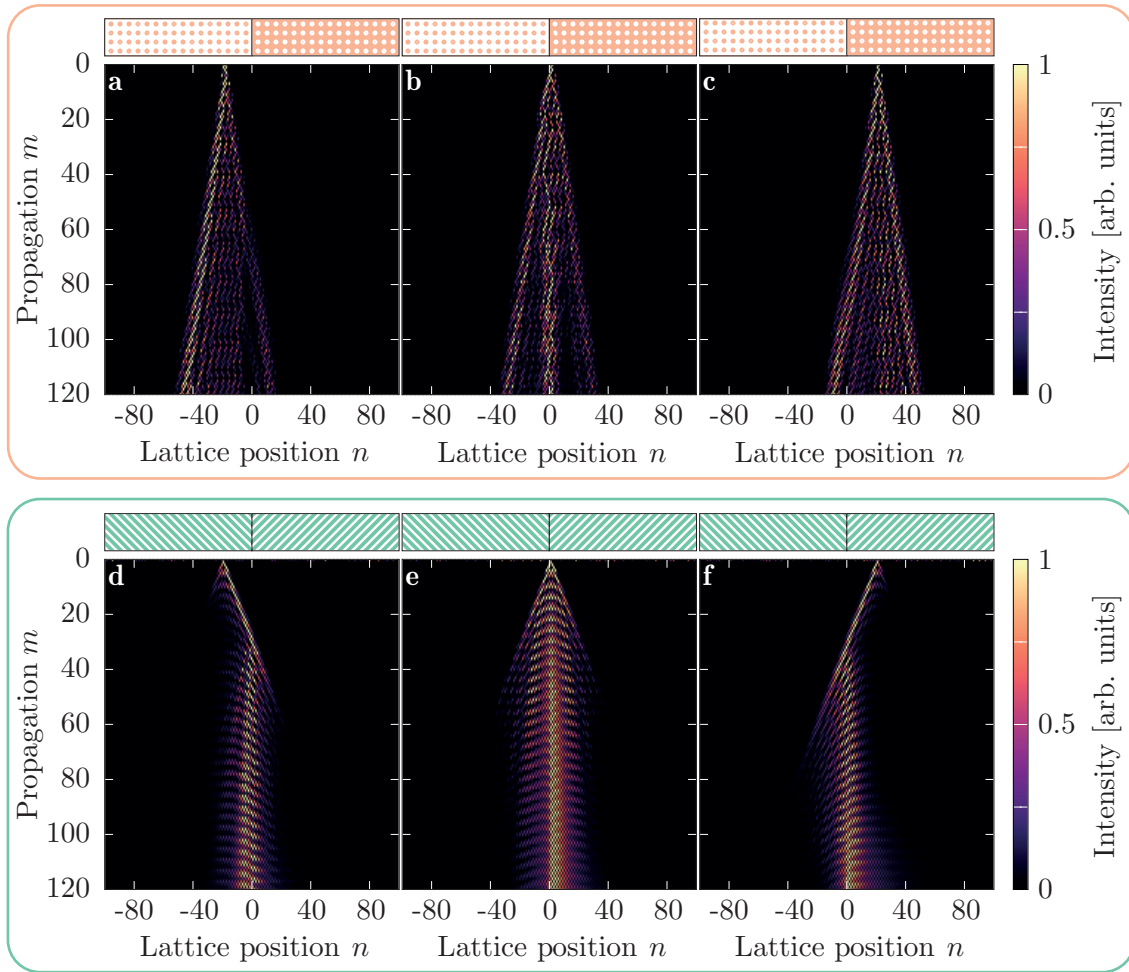


Figure 4.4 Experimental light propagation in the presence of a topological interface: **a** to **c**, The light intensity $|u_n^m|^2$ in the photonic lattice with the SSH modulation is shown upon exciting a single site either directly at the interface (**b**) or to its left (**a**) or right (**c**). **d** to **f**, The light propagation through the photonic lattice with the skin-effect modulation is shown upon exciting a single site either directly at the interface (**e**) or to its left (**d**) or right (**f**). The data represents the measured light intensity up to a normalization to the maximum value in each roundtrip, which is given by the arbitrary unit. Figure adapted from publication [W2].

4.3.3 Topological light funnelling

In the non-Hermitian lattice, all eigenstates are expected to localize at the interface, whereas in the SSH model, only one topological mode exists. To notably populate the topological mode in the SSH model, one therefore requires an excitation directly at (or in very close proximity to) the interface. However, in the non-Hermitian case, any excitation, irrespective of the input site, will propagate to the interface and localize there, which is exactly the topological light funnelling. The goal of the following experiments is to test the predicted topological eigenstate localization in lattices with asymmetric coupling via the resulting funnelling mechanism and to compare it to the Hermitian case, i.e., the SSH model.

The experiments start with probing the wave dynamics in the SSH model. According to Section 2.3, the topological interface is implemented by interchanging the beam splitting

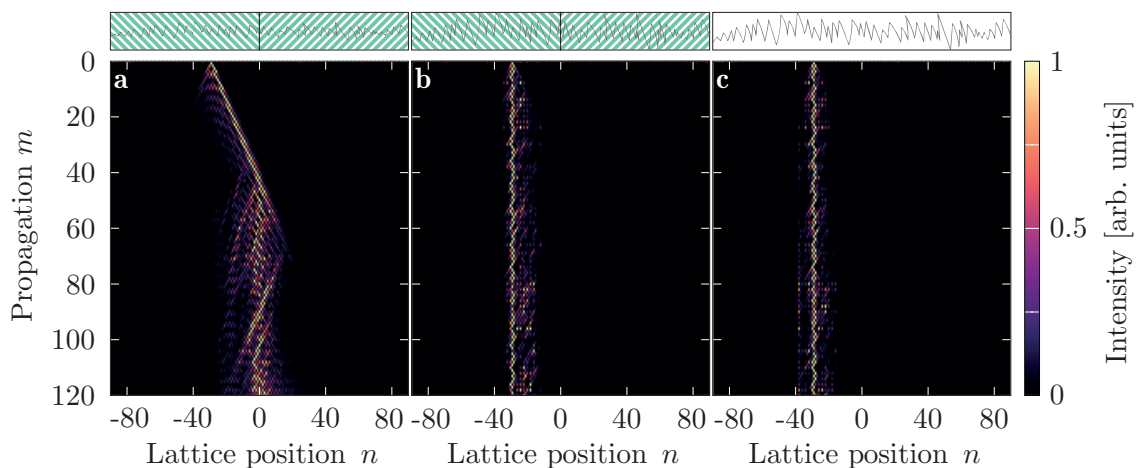


Figure 4.5 Topological robustness of the light funnelling: **a**, Experimental light propagation $|u_n^m|^2$ in the light-funnel lattice, but with additional phase disorder $W = 0.1\pi$. The grey line within the striped ribbons indicate that disorder is added, whereas a larger amplitude stands for a larger disorder strength. The light funnelling persists, even though the excitation is displaced to the left side of the interface. **b**, Same as in (a) but with stronger phase disorder, $W = 0.74\pi$. As a result, the funnelling breaks down and the wave dynamics show Anderson localization. **c**, Same as in (b) but without the asymmetric modulation, i.e., $\rho = 0$. The data represents the measured light intensity up to a normalization to the maximum value each roundtrip, which is given by the arbitrary unit. Figure adapted from publication [W2].

parameters β_1 and β_2 for all sites after some position. The composite lattice is excited at three different positions: left from the interface (Fig. 4.4a), directly at the interface (Fig. 4.4b), and right from the interface (Fig. 4.4c). Since the input does not perfectly match the topological eigenstate at the interface, also extended states are excited, which is clear from the corresponding spectrum (Fig. 4.2a). As a result, even when exciting at the interface, extended states lead to a spreading of the wave packet.

This situation is drastically different in the non-Hermitian model. The topological interface is realized by combining two lattices with inverted modulation with respect to the amplification and attenuation in Eq. (4.6). Here, any excitation results in a light flow that is directed toward the interface. This means it does not matter whether one excites displaced to the left from the interface (Fig. 4.4d), directly at the interface (Fig. 4.4e), or right from the interface (Fig. 4.4f). This light funnelling is a manifestation of the non-Hermitian skin effect, i.e., the eigenstate collapse at the interface shown in Fig. 4.2.

4.3.4 Robustness

To explore the robustness of the topological funnelling, disorder is applied to the real part of the on-site terms. To this end, the on-site phase terms $\phi_{u,n}^m$ are chosen as independent random variables for each site n , which are drawn from the same uniform distribution in the interval $[-W, W]$. In the experiments, the phase terms are applied via a phase modulator, as explained in Section 2.4. The experimental data shows that the topological light funnelling survives a certain amount of disorder, $W = 0.1\pi$, since the light still moves toward the interface (Fig. 4.5a). This demonstrates the topological robustness of the non-Hermitian skin effect. However, for sufficiently strong disorder, for instance

$W = 0.74\pi$, the light funnelling breaks down and Anderson localization is observed, i.e., the wave packet remains localized close to its origin (Fig. 4.5b). For comparison, the effect of Anderson localization is also shown for the Hermitian limit of the model, $\rho = 0$, in the case of strong disorder (Fig. 4.5c). The observed Anderson transition with a non-zero disorder threshold is a manifestation of the celebrated localization transition in the Hatano-Nelson model^[132], which therefore becomes topological: Whereas for weak disorder non-zero winding numbers are still possible, for strong disorder a topological transition occurs and the winding vanishes^[21].

4.3.5 Relation to current research and outlook

The non-Hermitian skin effect is meanwhile also realized via discrete-time quantum walks of single photons^[167], where instead non-Bloch topological invariants are used to establish a non-Hermitian bulk-boundary correspondence. The non-Hermitian skin effect was recently also observed in electric circuits^[168], where the Hamiltonian is implemented by an admittance matrix. Its Hermitian couplings originate from capacitive and inductive elements, whereas gain and loss are realized by operational amplifiers and serial resistances, respectively. In the electric circuit, the non-Hermitian skin effect manifests as a localization of all eigenstates of the admittance matrix upon changing from periodic to open boundaries.

The non-Hermitian skin effect model appears to be quantum-Hall-like topological phase in the sense that it does not require symmetry-protection^[21]. However, recent works suggest that there are also symmetry-protected non-Hermitian topological phases featuring a so-called \mathbb{Z}_2 skin effect, which is protected by time-reversal symmetry^[159].

In the perspective of technological directions it is an open task to identify more potential applications and to employ them in new devices. For example, topological sensors based on the non-Hermitian skin effect^[169] could be advanced in future works. Another recent proposal suggests selective and tunable excitations of laser modes with topological robustness based on the non-Hermitian skin effect^[170]. New devices might benefit from their topological robustness and their extreme sensitivity due to the non-Hermitian skin effect, or even from exotic features like self-healing of signals^[171].

Another direction involves the investigation of the non-Hermitian skin effect in aperiodic systems like quasicrystals, where the outcome of the interplay between aperiodic order, Hermitian localization transitions, and the non-Hermitian skin effect remains an open question, which is studied in Chapter 5.

5 Non-Hermitian topological quasicrystals

In this chapter, the interplay of aperiodic order, non-Hermitian topology and PT symmetry is investigated. It is shown that a topological, energy and localization phase transition can emerge from these ingredients, forming a *triple* phase transition. An experimental demonstration is presented in non-Hermitian Floquet quasicrystals, which are emulated in photonic discrete-time quantum walks. Before turning to the results of the corresponding publication [W3], a brief introduction into PT symmetry and 1D quasicrystals is provided.

5.1 PT symmetry

A milestone in the physics of non-Hermitian systems was the discovery by C.M. Bender and S. Boettcher^[11] that a large class of non-Hermitian Hamiltonians can exhibit entirely real spectra when they commute with the combined parity-time reversal (*PT*) operator. This statement was shown to hold not only for the *PT* operator, but instead any antiunitary operator A satisfying $A^{2k} = 1$ for some odd k can be used and it is therefore considered a generalized *PT* operator^[172]. A similar generalization is also described by the concept of pseudo-Hermiticity^[165]. The antiunitary operators can be represented in the form

$$A = UK, \tag{5.1}$$

where U is a unitary operator (e.g., P) and K is the complex conjugation (e.g., T). Fulfilling the commutation relation

$$[H, A] = 0 \tag{5.2}$$

guarantees that the eigenvalues of a non-Hermitian Hamiltonian H exist in complex conjugate pairs, though it is not a sufficient condition to assure that all eigenvalues are real. A completely real eigenvalue spectrum is guaranteed only in case of so-called unbroken (or exact) PT symmetry, i.e., when all eigenstates of the Hamiltonian are also eigenstates of the *PT* operator^[165]. As a result, certain non-Hermitian Hamiltonians exhibit a sharp symmetry-breaking transition: Once a certain system parameter exceeds a critical value, the Hamiltonian and the *PT* operator no longer have the same set of eigenstates even though the commutation relation remains unchanged. The eigenvalues of the Hamiltonian then branch into complex conjugate pairs and cease to be all real. This is the case of broken PT symmetry. Although in both PT phases the norm of the wavefunction can vary in time, its time-average is conserved in the unbroken phase, while it can exponentially grow in the broken phase^[173]. This distinctive feature is used in the following experiments to distinguish both phases.

Hamiltonians admitting PT symmetry are by now well established as an effective description of a multitude of dissipative systems and sparked numerous applications^[2,13,14]. The presence of PT symmetry has far reaching physical consequences also for topological systems. For instance, PT symmetry can prevent the existence of topological states^[3,174]. This is consistent with experiments observing topological states only in the case of broken PT symmetry^[163,164]. In contrast, other experiments demonstrate topological states protected by PT symmetry^[46], underlining the potential influence of non-Hermitian symmetries on topology^[3].

5.2 Phase transitions in quasicrystals

In all previous chapters, either spatially periodic or completely disordered structures have been discussed. However, materials can arrange themselves also in an intermediate phase, called *quasicrystals*, where lattice sites fill space in an ordered but aperiodic (quasiperiodic) way^[175]. Quasicrystals have attracted much attention since their discovery was reported in Dan Shechtmans Nobel Prize-winning work^[176] and their intriguing physical properties originate from their aperiodic order. A simple example for a 1D aperiodic sequence is

$$f_{\tau,\phi}(n) = \cos(2\pi n\tau + \phi), \quad (5.3)$$

which is a sampling, $n \in \mathbb{N}$, with frequency ν_s that is applied to a cosine signal with frequency ν , whereas their frequency ratio $\tau \equiv \nu/\nu_s$ must be an irrational number. In this case, one says that the two frequencies are incommensurable, and the aperiodic order results from the competition between the two length scales. The phase $\phi \in \mathbb{R}$ denotes an additional degree of freedom, which will be discussed below.

A paradigmatic model with aperiodic order in 1D is the AUBRY–ANDRÉ–HARPER (AAH) model^[177–179]. It consists of a linear chain of nearest-neighbour coupled sites and its Hamiltonian exhibits an additional spatial modulation of the on-site terms that is proportional to $f_{\tau,\phi}(n)$, with n denoting the lattice sites. Although being one-dimensional, the AAH model displays a delocalization-localization phase transition at a finite value of the modulation amplitude^[105,180]. Moreover, at the phase transition point, the energy spectrum is governed by the Harper equation^[178], which describes the motion of an electron on a 2D square lattice that is subject to a perpendicular magnetic field and gives rise to the famous Hofstadter butterfly energy spectrum^[179]. This connection between the AAH model and the 2D quantum Hall (Harper-Hofstadter) system has been experimentally tested and can be explained in terms of the non-trivial topology of the AAH model, which is related to the phase degree of freedom, ϕ , in Eq. (5.3)^[32,181,182].

Recent works suggest that quasicrystals exhibit non-Hermitian topological phases^[183–189]. For instance, by considering a PT symmetric extension of the AAH model, a localization-delocalization transition is predicted to coincide with the PT symmetry breaking point, and the phase transition encompasses two distinct topological phases^[186]. The corresponding topological invariant characterizes the spectral winding of the energy eigenvalues in the complex plane, akin to Eq. (4.1) employed in Chapter 4, but it is adapted to be applicable to quasicrystals, i.e., settings without spatial translation symmetry^[21]. To this end, an additional phase degree of freedom is employed, being conceptually similar to ϕ in Eq. (5.3).

5.3 Results

In this section, the results of the publication [W3] are presented. Based on 1D quantum walks it is theoretically and experimentally shown that eigenstate localization, PT symmetry breaking, and a non-Hermitian topological phase transition can be mutually interlinked in a non-Hermitian Floquet quasicrystal. The model supports the non-Hermitian skin effect with a non-trivial point gap topology, as introduced in Chapter 4. The topological phase transition, the localization phase transition, and the spontaneous PT-symmetry breaking coincide and thus form a topological triple phase transition. The transition is induced by changing a single system parameter, which can be the strength of the nearest-neighbour coupling or strength of the non-Hermiticity, both of which are connected in a phase transition equation. In the Hermitian limit, a Floquet version of the AAH model is obtained, showing a Hofstadter butterfly quasienergy spectrum.

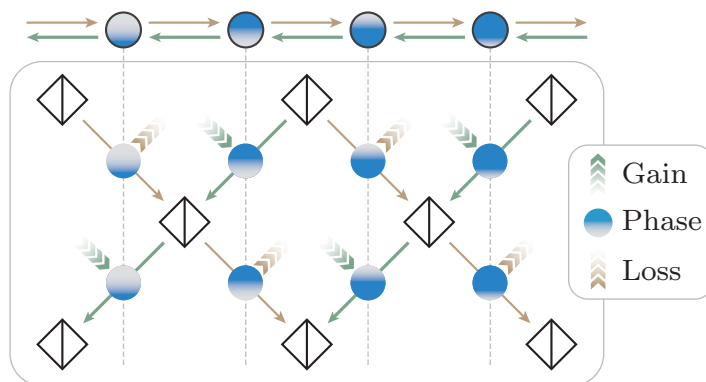


Figure 5.1 Non-Hermitian Floquet AAH model: A one-dimensional chain of sites (top) is realized via a discrete-time quantum walk of light in a mesh lattice of beam splitters (bottom) that is created by coupled optical fibre loops (see Chapter 2). The on-site phase terms $\phi_{u,n}^m$ and $\phi_{v,n}^m$ (local value and sign correspond to amount and orientation of the blue coloured fillings, respectively) form spatial phase gradients whose sign depends on the hopping direction, thereby yielding the Hermitian Floquet AAH model. By adding the gain-loss modulation from the non-Hermitian skin effect model (see Chapter 4), one obtains the non-Hermitian Floquet AAH model. Figure adapted from publication [W3].

5.3.1 Non-Hermitian photonic quasicrystals

In a first step, a Floquet version of the AAH model is introduced, which is based on 1D discrete-time quantum walks as defined by Eq. (2.5). In a second step, a non-Hermitian skin effect modulation is included so that the model exhibits PT symmetry.

The starting point for the time-discrete AAH model is the introduction of on-site phase terms

$$\phi_{u,n}^m = (-1)^m \left(n + \frac{1}{2} \right) \frac{\pi\varphi}{2}, \quad \phi_{v,n}^m = (-1)^{m+1} \left(n - \frac{1}{2} \right) \frac{\pi\varphi}{2}, \quad (5.4)$$

to a lattice with constant nearest-neighbour coupling $\beta_n^m \equiv \beta$, whereas φ is an irrational number in order to be incommensurate to the spacing of lattice sites $n = 1 \dots N$.

At the critical point of the original AAH model, the energy spectrum is governed by the Harper equation^[178] and in the corresponding model considered by Harper, the influence of the magnetic field is captured by spatial phase gradients (Peierls phase) whose sign depends on the hopping direction. This is reflected by the spatial gradients with opposite signs in the on-site phase terms for the left- and right-moving components $\phi_{u,n}^m$ and $\phi_{v,n}^m$, respectively. An additional sign-flip in each time step m accounts for the sublattice structure of the quantum walk and assures that equal phase terms are vertically aligned in the (1+1)D lattice (see Fig. 5.1).

For the non-Hermitian extension, the amplitude modulation

$$G_{u,n}^m = \exp(h), \quad G_{v,n}^m = \exp(-h), \quad (5.5)$$

is added, and it resembles the non-Hermitian skin effect modulation, Eq. (4.6), with the non-Hermiticity (gain-loss) parameter $h \in \mathbb{R}$. By combining the quasiperiodic phase potential in Eq. (5.4) with the non-Hermitian contribution in Eq. (5.5), the desired non-Hermitian Floquet AAH model is formed.

In the following, the potential frequency is chosen to be the inverse of golden mean, i.e., the irrational number $\varphi = (\sqrt{5} - 1)/2$.

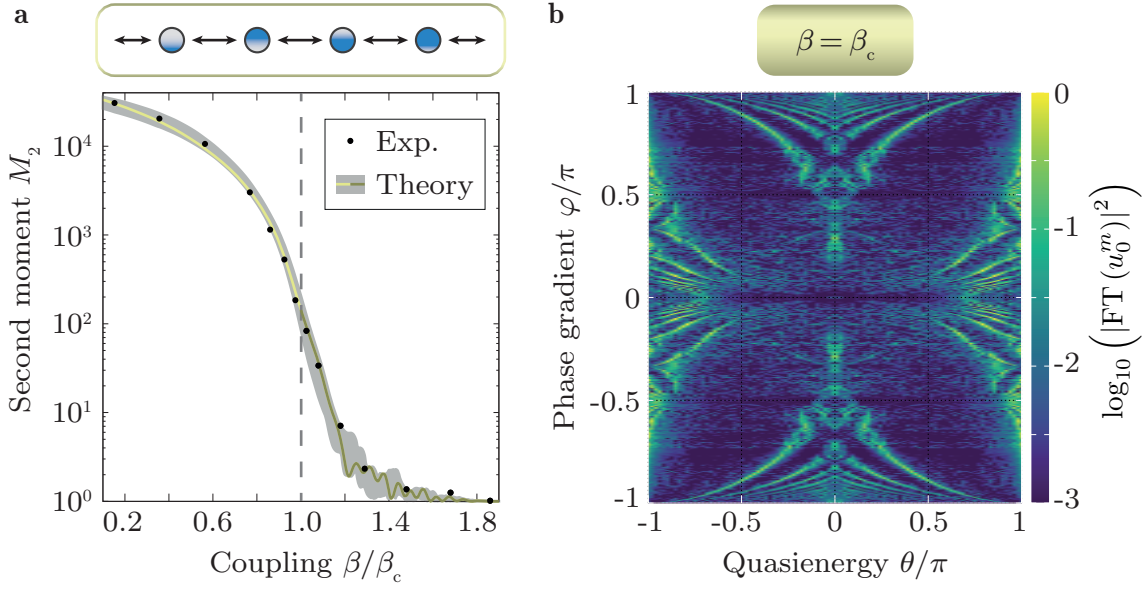


Figure 5.2 Metal–insulator phase transition and Hofstadter butterfly in the Floquet AAH model: **a**, The spatial spreading of the wavefunction is shown via the second spatial moment, Eq. (3.2), after $m = 200$ time steps. The lattice was excited with a single-site excitation. The grey area marks the tolerance region, which displays expected deviations owing to limited accuracy in the lattice parameters (see Methods in [W3]). The experimental data shows a dramatic spatial wave localization upon increasing the inter-site coupling parameter beyond $\beta_c = \pi/4$. This is exactly the predicted metal-insulator phase transition, which also occurs in the original AAH model. **b**, At the transition point, β_c , the time-discrete Floquet analogue of the Hofstadter–Harper model emerges. The quasienergies θ are retrieved from the propagation data after $m = 380$ time steps, by evaluating the temporal Fourier transform (FT) of the site amplitudes (see SI of [W3]). Here, $|u_0^m|$ is retrieved from the intensity measurement. The lost phase information, which are only \pm signs due to symmetry, is supplied based on Eq. (2.5). The experiment was conducted for 200 different phase gradients φ . Figure adapted from publication [W3].

5.3.2 Floquet Hofstadter butterfly

In the Hermitian limit, $h = 0$, the presented model displays a localization (metal-insulator) phase transition when increasing the inter-site coupling beyond the critical point $\beta_c = \pi/4$. This follows from a numerical eigenstate analysis (see SI of [W3]), which shows that for $\beta < \beta_c$ all eigenstates are extended, while for $\beta > \beta_c$ all eigenstates are exponentially localized. Moreover, one finds that all eigenstates have the same localization length, Eq. (3.1), which is a characteristic feature of the original AAH model, and its inverse γ is well approximated by

$$\gamma = \log \left(1 + \frac{1}{\cos(\beta)} - \frac{1}{\cos(\pi/4)} \right). \quad (5.6)$$

The value of the phase transition point, β_c , can be derived rigorously by a self-duality argumentation (see SI of [W3]), similar to the one applied in the original AAH model^[177,190]. Remarkably, at the phase transition point, the quasienergy spectrum forms a Floquet version of the Harper–Hofstadter butterfly when displaying the possible energy levels over the phase gradient φ ^[82]. The wording *Floquet* Hofstadter butterfly is used because its fractal structure arises from the two-step Floquet dynamics.

Before turning to the non-Hermitian model, the Hermitian one is experimentally tested¹: The delocalization-localization phase transition and the Floquet Hofstadter butterfly are reproduced well in the experimental data (see Fig. 5.2).

A natural question that arises for any experimental result is how the limited experimental accuracy affects the implementation of an irrational phase gradient φ , because from a theoretical point of view, the energy spectrum and localization properties strongly depend on whether φ is rational or irrational. On one hand, one expects a smooth transition of the energy spectrum when approaching the irrational frequency^[179], for instance via the rational quotients $\varphi = \lim_{l \rightarrow \infty} p_l/q_l$ with p_l being the sequence of Fibonacci numbers and $q_l = p_{l+1}$. On the other hand, one has to consider that in any experiment one deals with a finite number of lattice sites and a finite observation time T , which is here the maximum number of time steps. Owing to the time-energy uncertainty, one cannot resolve the spectral features observed (for example the fractal structure of Hofstadter's butterfly) with an arbitrarily high resolution when approaching the irrational φ . Within $m = T$ time steps one never probes more than $L = T$ sites at the left and right sides from a single-site excitation. Therefore, the experiment would effectively yield the same results for a deviating gradient $\varphi \pm \Delta\varphi$ when $\Delta\varphi$ is smaller than $1/T$. The experimentally achieved relative error for the phase modulation is better than 1% and such a deviation does not significantly affect the results, as for instance displayed by the grey areas in Fig. 5.2 and Fig. 5.3, which account for such deviations.

5.3.3 Topological triple phase transition

In the non-Hermitian case, $h \neq 0$, the model exhibits a topological triple phase transition (Fig. 5.3) at a critical point $\beta_n^m = \beta_c$, which can be related to the critical gain-loss strength $h = h_c$ by

$$h_c = \log \left(1 + \frac{1}{\cos(\beta_c)} - \frac{1}{\cos(\pi/4)} \right), \quad (5.7)$$

as explained below. One can clearly see that the derivation is based on the localization lengths of the Hermitian model, Eq. (5.6). Upon applying the amplitude transformation

$$u_n^m \rightarrow u_n^m e^{-hn}, \quad v_n^m \rightarrow v_n^m e^{hn}, \quad (5.8)$$

one obtains the Hermitian case. Now suppose h is used as a control parameter. For $h = 0$, one expects the metal-insulator transition at $\beta_c = \pi/4$. Starting in the localized phase $\beta < \beta_c$, while slightly increasing $h > 0$, one obtains an asymmetric spatial localization of modes, as is clear from Eq. (5.8). However, at the critical point $h = \gamma$, the exponential increase of the amplitude counterbalances the exponential localization. Remarkably, all eigenstates are affected because in the (Floquet) AAH model all eigenstates have the same localization length. As a result, a metal-insulator phase transition is induced by changing h beyond the value of the inverse localization length, which in turn depends on β . The non-Hermitian phase transition equation suggests that the transition also occurs when changing the coupling beyond a critical point $\beta_c(h)$ for a fixed coupling asymmetry strength h , which will be verified in the following experiments (Fig. 5.3).

¹In the experiments, the phase modulation in Eq. (5.4) is adapted to the form $\phi_{n,v}^m = 0$ and $\phi_{n,u}^m = (-1)^m n\pi\varphi$, which requires a phase modulation only in the shorter fibre loop. The adapted modulation yields the same result because the lattice symmetry and the relative phases between both loops are maintained, which was also verified numerically.

Besides the localization transition, which is now situated at $\beta_c(h)$, a PT symmetry breaking takes place at the same value, separating the PT broken phase ($\beta < \beta_c$), which shows an exponential growth of the overall energy, from the PT unbroken phase ($\beta > \beta_c$), where the energy exchange with the environment is on time-average balanced. The overall energy is defined by $\sum_n |u_n^m|^2 + |v_n^m|^2$, which in the experiments corresponds to the total light intensity in both fibre loops. By applying a suitable change of basis, one can show that the Floquet AAH model admits PT symmetry with $P = \sigma_i$ and $T = \sigma_i K$, whereas σ_i denotes one of the Pauli matrices and K complex conjugation (see SI of [W3]).

The third transition that occurs at β_c is a topological one, in which the spectral winding of the complex quasienergies changes. The corresponding winding number w for a lattice with aperiodic order is defined as follows. For any rational approximation of the irrational phase gradient, $\varphi_l = p_l/q_l$, the time-evolution operator admits spatial translation symmetry with period $L = 2q_l$. When considering the corresponding Bloch Hamiltonian with L sites and periodic boundary conditions, one can define a topological winding number upon introducing a magnetic flux^[21], which adds to the phase modulation, Eq. (5.4), in the form

$$\phi_{u,n}^m \rightarrow \phi_{u,n}^m + \frac{\vartheta}{2L}, \quad \phi_{v,n}^m \rightarrow \phi_{v,n}^m - \frac{\vartheta}{2L}, \quad (5.9)$$

where ϑ is proportional to the magnitude of the magnetic flux. As a result, $\det(H(\vartheta/L))$ becomes 2π -periodic in ϑ and the corresponding spectral winding is given by^[21,186,189]

$$w(h) = \lim_{L \rightarrow \infty} \frac{1}{2\pi i} \int_0^{2\pi} \frac{\partial}{\partial \vartheta} \log \det \left(H \left(\frac{\vartheta}{L}, h \right) - \mathbb{1}_{\theta_B} \right) d\vartheta, \quad (5.10)$$

which counts the number of times the complex spectral trajectory encircles a base point quasienergy, here $\theta_B = 0$, when the phase ϑ is varied from 0 to 2π .

In the last experiment, the three phase transitions are probed. To this end, the coupling β is varied for the fixed gain-loss strength $h = 0.12$. According to the non-Hermitian phase transition relation, Eq. (5.7), the critical coupling is $\beta_c = 1.1\pi/4$, i.e., it is shifted away from the symmetry point of the Hermitian model. The results in Fig. 5.3 show that the system undergoes three phase transitions at the critical point β_c . For $\beta < \beta_c$, eigenstates are spatially extended and the energy spectrum forms closed loops in the complex plane, which are characterized by a non-zero winding number, and the PT symmetry is broken. Conversely, for $\beta > \beta_c$, all eigenstates become exponentially localized, PT symmetry is unbroken and all eigenvalues become real, i.e., the energy gaps close and the winding number vanishes.

To verify the change of the winding number, the wave propagation is considered (Fig. 5.4). From the onset of the non-Hermitian skin effect, which is deduced from the biased transport in the bulk as visible far away from the interface, one can infer a non-zero winding^[191], as numerically predicted (Fig. 5.3, top row). In contrast, the skin effect is suppressed in the localized phase, from which one can deduce $w = 0$, i.e., a topologically trivial phase^[21,191]. Moreover it was numerically verified that, as in the experiments, the light localization at the interface occurs only if the adjacent media have different winding numbers, supporting the potential existence of a non-Hermitian bulk–boundary correspondence in quasicrystals. The overall results show that all three phase transitions coincide at $\beta_c = 1.1\pi/4$, yielding the predicted topological triple phase transition.

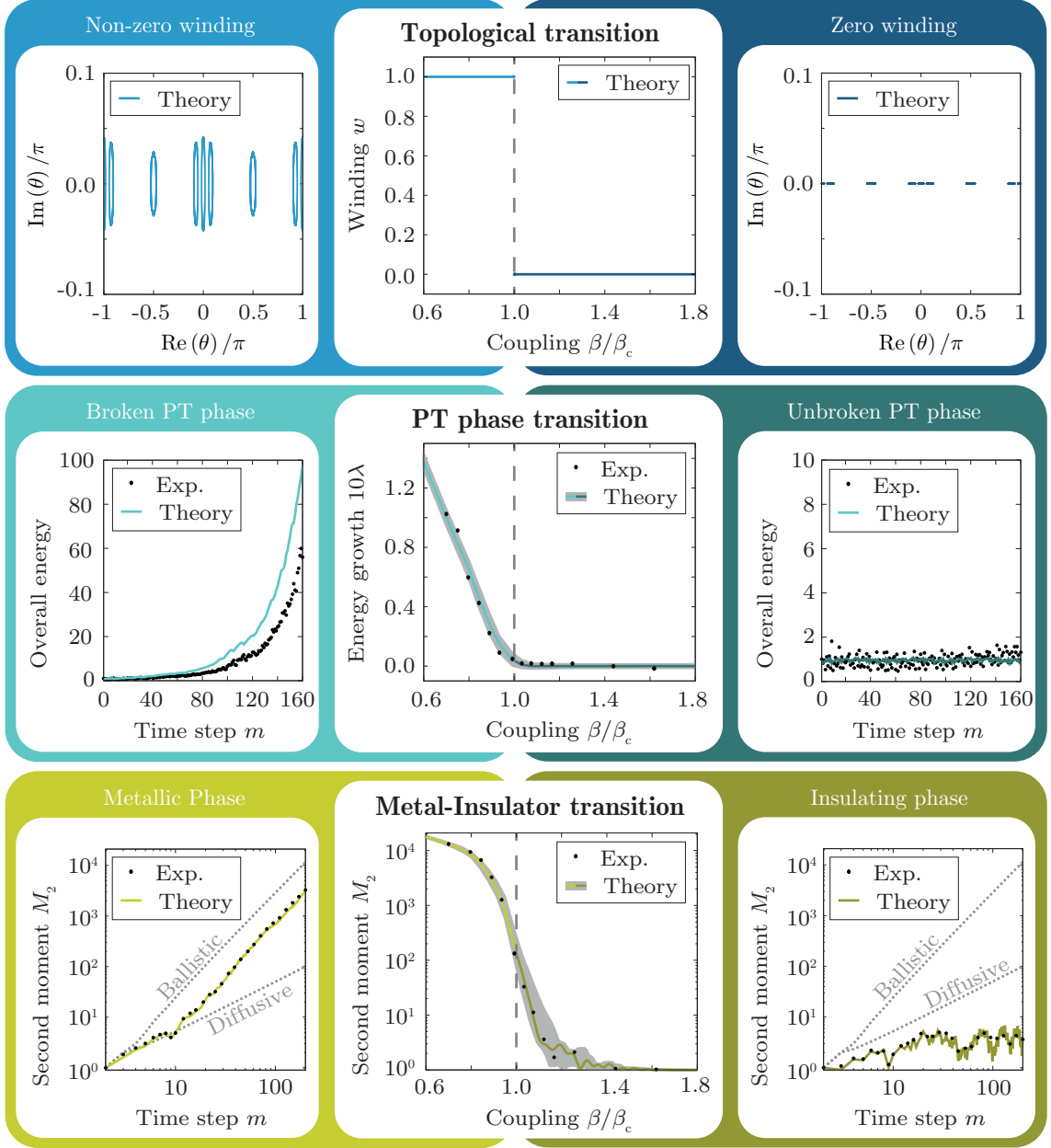


Figure 5.3 Topological triple phase transition: Three phase transitions are arranged row-wise. The left column corresponds to $\beta = 0.89\beta_c$, whereas the right column corresponds to $\beta = 1.12\beta_c$. Top row: The system is topologically non-trivial owing to the formation of point-energy gaps with non-zero winding (left). At β_c the topological phase changes, as the spectrum becomes real and the winding vanishes (right). Centre row: The quasicrystal is in the broken PT phase (left), which is marked by an exponential growth, of the overall energy $\sum_n |u_n^m|^2 + |v_n^m|^2 \propto e^{\lambda m}$ in time m . At β_c the system changes to the unbroken PT phase (right), where the overall energy becomes on time-average constant. Bottom row: The quasicrystal is in the delocalized phase (left), which is marked by the monotonic increase of the second spatial moment M_2 in time, Eq. (3.2). At the phase transition point, all eigenstates become exponentially localized, which is indicated by the extremely low second moment. All experiments start with a single-site excitation. The grey areas mark the tolerance regions of expected deviations due to the limited accuracy in the lattice parameters (see Methods in [W3]). Figure adapted from publication [W3].

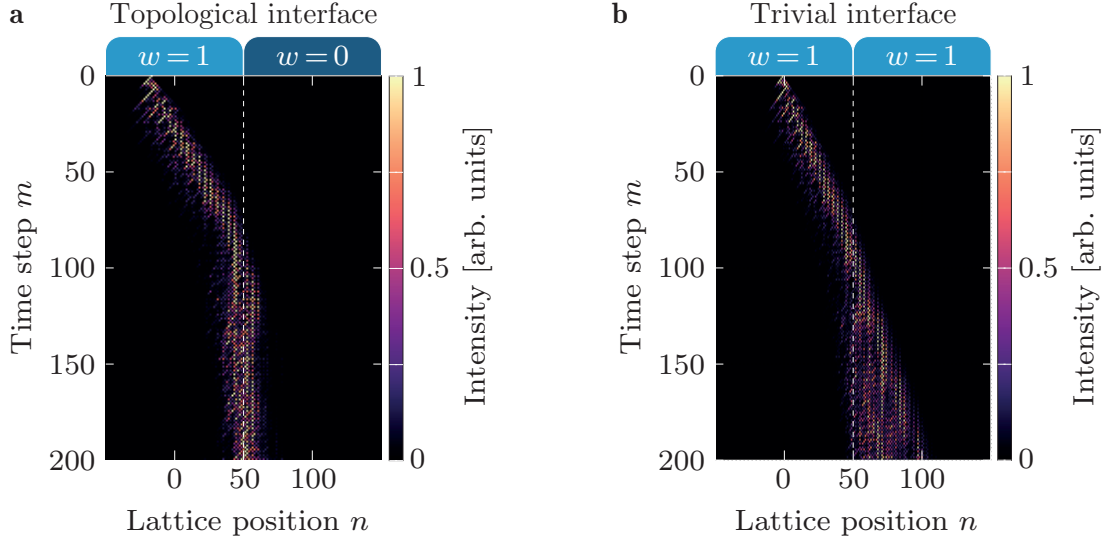


Figure 5.4 Topological and trivial interface: **a**, Light localization is observed at a topological interface with $\beta = 0.70\beta_c$ on the left and $\beta = 1.03\beta_c$ on the right side of the interface, respectively. The corresponding winding numbers $w(\beta)$ are shown above. **b**, Light does not localize at a topologically trivial interface with $\beta = 0.70\beta_c$ on the left and $\beta = 0.89\beta_c$ on the right side of the interface, respectively. The data represents the measured light intensity $|u_n^m|^2$ up to a normalization to the maximum value each roundtrip, which is given by the arbitrary unit. Figure adapted from publication [W3].

5.3.4 Relation to current research and outlook

The results discussed in this chapter demonstrate the interconnectedness of non-Hermitian topology, PT symmetry and localization in non-Hermitian Floquet quasicrystals. Another experimental work was published afterwards and demonstrated a similar connection based on discrete-time quantum walks of single photons^[192], whereas the propagation was limited to ten time steps only. Further realizations with mode-locked lasers^[193] or electric circuits^[183] have been proposed. Future works might investigate if and under which general conditions topology, (PT) symmetry, and eigenstate localization are mutually interlinked, as presented here. Inspired by the higher-dimensional topology of lower-dimensional quasicrystals^[175], it might be likewise possible to realize higher-dimensional non-Hermitian topological phases in lower-dimensional non-Hermitian quasicrystals.

In the perspective of potential technical applications, the results could pave the way for novel phase-change devices, in which not only edge and bulk transport but also the energy and particle exchange with the environment (dissipation) can be controlled and predicted by the topological phase and vice versa.

Regarding the Floquet version of the Harper-Hofstadter butterfly emerging in discrete-time quantum walks, recent works have shown that the corresponding quasienergy spectrum can indeed form a zero-measure Cantor set^[194], which is a distinguished feature of the original static model.

6 Conclusion

In this thesis, the interplay between topology, disorder, and dissipation was investigated based on a photonic implementation of one-dimensional discrete-time quantum walks. Throughout this thesis, combinations of three major fields were discussed: Topology, the influence of dissipation, and systems with disorder or aperiodic order. Firstly, the interplay of disorder and dissipation was investigated, introducing a novel non-Hermitian eigenstate localization in coexistence with dynamical delocalization. Secondly, a disorder-robust light-guiding mechanism was presented, based on non-Hermitian topological phases. Thirdly, all previous ingredients were combined to form a non-Hermitian topological system with aperiodic order, where an interconnectedness of topology, eigenstate localization, and PT symmetry was observed. In all three works, the combination of dissipation with concepts from other fields of physics lead to surprising new results, which were observed in the chosen experimental platform.

The first work investigated the impact of uncorrelated, stochastic dissipation on the single-particle wave dynamics. It was shown that such disorder can lead to an exponential localization of all eigenstates, as in the case of Anderson localization in Hermitian systems. However, in sharp contrast, the measured light distributions still showed a spatial spreading as if the underlying eigenstates were extended, which is a novel non-Hermitian phenomenon resulting from the stochastic distribution of lifetimes and the post-selection of dissipated photons. This coexistence of spectral localization and dynamical delocalization was theoretically described and experimentally demonstrated.

For the second project, topological phases exclusive to non-Hermitian systems were studied, based on Hamiltonians with asymmetric coupling. The topological phases were described by winding numbers of the energy eigenvalues in the complex plane, and by interfacing two systems with different winding numbers, a topological funnelling of light was observed: All eigenstates were localized at the interface, i.e., any light field that impinges the system is guided toward the funnel opening, independently of the input shape and position. These observations were markedly different from the presented results on the SSH model, which is an archetypical model for Hermitian topology, where only one topological state emerges. The robustness of the non-Hermitian topological light guiding was experimentally tested and revealed that upon exceeding a critical disorder strength, Anderson localization is observed. This result is a manifestation of the celebrated localization transition in the Hatano-Nelson model, which therefore gained a topology-based interpretation.

The third project was dedicated to the topological phases of non-Hermitian quasicrystals, with the starting point being a Floquet version of the Aubry-André-Harper model. It was predicted that the interplay between the emergent non-Hermitian topology, aperiodic order, and PT symmetry leads to the formation of a triple phase transition: The PT symmetry induces a transition to an on time-average preserved light intensity, and it is mutually interlinked with a topological one as the complex energy gap closed at the critical point. Finally, a delocalization-localization transition, i.e., Anderson localization, occurred at the same critical coupling parameter, which was shifted away from the self-dual point of the Hermitian model owing to the asymmetric couplings. Moreover, in the Hermitian limit, a novel Floquet version of Hofstadter's butterfly was observed. The results demonstrated an interconnectedness of non-Hermitian topology, bulk transport, and PT symmetry.

In the way of attaining the presented results, the coupled optical fibre loops have proven to be a versatile experimental platform for studying non-Hermitian physics. Nevertheless,

the single spatial dimension limits the range of accessible phenomena. Experimental works have shown that the coupled optical fibre loops can be extended to emulate two or more spatial dimensions^[195,196], therefore being a promising platform also for higher-dimensional phenomena. Moreover, a degree of freedom not used in this thesis is the accumulation of nonlinear phase shifts due to optical self-phase modulation^[81,197]. In combination with the presented results, the experimental platform might pave the way toward emulating dissipative systems with interactions, thereby accessing a whole new class of phenomena that might also host non-Hermitian counterparts to the fractional quantum Hall states.

While the findings of this thesis extended the theoretical and experimental basis for the study of the interplay of topology, disorder, and dissipation, they have also opened up new questions. For instance, can non-Hermitian point-gap topology, bulk transport, and non-Hermitian symmetries be united in a generalised concept? Will realistic devices based on non-Hermitian point-gap topology outperform their Hermitian counterparts? Are there novel anomalous Floquet non-Hermitian topological phases? This appears to be a fertile ground for future investigations and discoveries.

List of all publications

Journal articles

- [W1] [S. Weidemann](#), M. Kremer, S. Longhi, and A. Szameit *Coexistence of dynamical delocalization and spectral localization through stochastic dissipation*, Nature Photonics **15**, 576 (2021).
- [W2] [S. Weidemann](#), M. Kremer, T. Helbig, T. Hofmann, A. Stegmaier, M. Greiter, R. Thomale, and A. Szameit *Topological funneling of light*, Science **368**, 311 (2020).
- [W3] [S. Weidemann](#), M. Kremer, S. Longhi, and A. Szameit *Topological triple phase transition in non-Hermitian Floquet quasicrystals*, Nature **601**, 354 (2022).
- [W4] A. Dikopoltsev, [S. Weidemann](#), M. Kremer, A. Steinfurth, H. Sheinflux, A. Szameit, and M. Segev *Observation of Anderson localization beyond the spectrum of the disorder*, Science Advances **8**, eabn7769 (2022).
- [W5] A. Steinfurth, I. Krešić, [S. Weidemann](#), M. Kremer, K. Makris, M. Heinrich, S. Rotter, and A. Szameit *Observation of photonic constant-intensity waves and induced transparency in tailored non-Hermitian lattices*, Science Advances **8**, eab17412 (2022).

Bibliography

- [1] H.-P. Breuer and F. Petruccione, *The Theory of Open Quantum Systems* (Oxford University Press, New York, 2002).
- [2] R. El-Ganainy, K. G. Makris, M. Khajavikhan, Z. H. Musslimani, S. Rotter, and D. N. Christodoulides, *Nature Physics* **14**, 11 (2018).
- [3] K. Kawabata, K. Shiozaki, M. Ueda, and M. Sato, *Phys. Rev. X* **9**, 041015 (2019).
- [4] Y. Ashida, Z. Gong, and M. Ueda, *Advances in Physics* **69**, 249 (2020).
- [5] C. M. Bender, *Reports on Progress in Physics* **70**, 947 (2007).
- [6] I. Rotter, *Journal of Physics A: Mathematical and Theoretical* **42**, 153001 (2009).
- [7] N. Moiseyev, *Non-Hermitian Quantum Mechanics* (Cambridge University Press, 2011).
- [8] M. V. Berry, *Czechoslovak Journal of Physics* **54**, 1039 (2004).
- [9] W. D. Heiss, *Journal of Physics A: Mathematical and General* **37**, 2455 (2004).
- [10] M.-A. Miri and A. Alù, *Science* **363**, eaar7709 (2019).
- [11] C. M. Bender and S. Boettcher, *Phys. Rev. Lett.* **80**, 5243 (1998).
- [12] A. Mostafazadeh, *International Journal of Geometric Methods in Modern Physics* **07**, 1191 (2010).
- [13] L. Feng, R. El-Ganainy, and L. Ge, *Nature Photonics* **11**, 752 (2017).
- [14] S. K. Özdemir, S. Rotter, F. Nori, and L. Yang, *Nature Materials* **18**, 783 (2019).
- [15] C. E. Rüter, K. G. Makris, R. El-Ganainy, D. N. Christodoulides, M. Segev, and D. Kip, *Nature Physics* **6**, 192 (2010).
- [16] A. Regensburger, C. Bersch, M.-A. Miri, G. Onishchukov, D. N. Christodoulides, and U. Peschel, *Nature* **488**, 167 (2012).
- [17] W. Chen, S. Kaya Oezdemir, G. Zhao, J. Wiersig, and L. Yang, *Nature* **548**, 192 (2017).
- [18] H. Hodaei, A. U. Hassan, S. Wittek, H. Garcia-Gracia, R. El-Ganainy, D. N. Christodoulides, and M. Khajavikhan, *Nature* **548**, 187 (2017).
- [19] H. Hodaei, M.-A. Miri, M. Heinrich, D. N. Christodoulides, and M. Khajavikhan, *Science* **346**, 975 (2014).
- [20] L. Feng, Z. J. Wong, R.-M. Ma, Y. Wang, and X. Zhang, *Science* **346**, 972 (2014).
- [21] Z. Gong, Y. Ashida, K. Kawabata, K. Takasan, S. Higashikawa, and M. Ueda, *Phys. Rev. X* **8**, 031079 (2018).
- [22] B. A. Bernevig, *Topological Insulators and Topological Superconductors* (Princeton University Press, 2013).

- [23] J. K. Asbóth, L. Oroszlány, and A. Pályi, *Lecture notes in physics* **919**, 166 (2016).
- [24] M. Nakahara, *Geometry, topology and physics* (CRC press, 2018).
- [25] D. J. Thouless, M. Kohmoto, M. P. Nightingale, and M. den Nijs, *Phys. Rev. Lett.* **49**, 405 (1982).
- [26] M. Z. Hasan and C. L. Kane, *Rev. Mod. Phys.* **82**, 3045 (2010).
- [27] X.-L. Qi and S.-C. Zhang, *Rev. Mod. Phys.* **83**, 1057 (2011).
- [28] C.-K. Chiu, J. C. Y. Teo, A. P. Schnyder, and S. Ryu, *Rev. Mod. Phys.* **88**, 035005 (2016).
- [29] N. P. Armitage, E. J. Mele, and A. Vishwanath, *Rev. Mod. Phys.* **90**, 015001 (2018).
- [30] Z. Wang, Y. Chong, J. D. Joannopoulos, and M. Soljačić, *Nature* **461**, 772 (2009).
- [31] M. C. Rechtsman, J. M. Zeuner, Y. Plotnik, Y. Lumer, D. Podolsky, F. Dreisow, S. Nolte, M. Segev, and A. Szameit, *Nature* **496**, 196 (2013).
- [32] Y. E. Kraus, Y. Lahini, Z. Ringel, M. Verbin, and O. Zilberberg, *Phys. Rev. Lett.* **109**, 106402 (2012).
- [33] L. Lu, J. D. Joannopoulos, and M. Soljačić, *Nature Photonics* **8**, 821 (2014).
- [34] T. Ozawa, H. M. Price, A. Amo, N. Goldman, M. Hafezi, L. Lu, M. C. Rechtsman, D. Schuster, J. Simon, O. Zilberberg, and I. Carusotto, *Rev. Mod. Phys.* **91**, 015006 (2019).
- [35] S. D. Huber, *Nature Physics* **12**, 621 (2016).
- [36] G. Ma, M. Xiao, and C. T. Chan, *Nature Reviews Physics* **1**, 281 (2019).
- [37] J. Ningyuan, C. Owens, A. Sommer, D. Schuster, and J. Simon, *Phys. Rev. X* **5**, 021031 (2015).
- [38] C. H. Lee, S. Imhof, C. Berger, F. Bayer, J. Brehm, L. W. Molenkamp, T. Kiessling, and R. Thomale, *Communications Physics* **1**, 39 (2018).
- [39] N. Goldman, J. C. Budich, and P. Zoller, *Nature Physics* **12**, 639 (2016).
- [40] M. Lohse, C. Schweizer, H. M. Price, O. Zilberberg, and I. Bloch, *Nature* **553**, 55 (2018).
- [41] P. Delplace, J. B. Marston, and A. Venaille, *Science* **358**, 1075 (2017).
- [42] S. Yao and Z. Wang, *Phys. Rev. Lett.* **121**, 086803 (2018).
- [43] M. A. Bandres, S. Wittek, G. Harari, M. Parto, J. Ren, M. Segev, D. N. Christodoulides, and M. Khajavikhan, *Science* **359**, eaar4005 (2018).
- [44] A. Cerjan, S. Huang, M. Wang, K. P. Chen, Y. Chong, and M. C. Rechtsman, *Nature Photonics* **13**, 623 (2019).
- [45] H. Zhao, P. Miao, M. H. Teimourpour, S. Malzard, R. El-Ganainy, H. Schomerus, and L. Feng, *Nature Communications* **9**, 981 (2018).

-
- [46] S. Weimann, M. Kremer, Y. Plotnik, Y. Lumer, S. Nolte, K. G. Makris, M. Segev, M. C. Rechtsman, and A. Szameit, *Nature Materials* **16**, 433 (2017).
- [47] M. Parto, S. Wittek, H. Hodaei, G. Harari, M. A. Bandres, J. Ren, M. C. Rechtsman, M. Segev, D. N. Christodoulides, and M. Khajavikhan, *Phys. Rev. Lett.* **120**, 113901 (2018).
- [48] L. Xiao, X. Zhan, Z. H. Bian, K. K. Wang, X. Zhang, X. P. Wang, J. Li, K. Mochizuki, D. Kim, N. Kawakami, W. Yi, H. Obuse, B. C. Sanders, and P. Xue, *Nature Physics* **13**, 1117 (2017).
- [49] H. Zhou, C. Peng, Y. Yoon, C. W. Hsu, K. A. Nelson, L. Fu, J. D. Joannopoulos, M. Soljacic, and B. Zhen, *Science* **359**, 1009 (2018).
- [50] J. M. Zeuner, M. C. Rechtsman, Y. Plotnik, Y. Lumer, S. Nolte, M. S. Rudner, M. Segev, and A. Szameit, *Phys. Rev. Lett.* **115**, 040402 (2015).
- [51] A. Regensburger, C. Bersch, B. Hinrichs, G. Onishchukov, A. Schreiber, C. Silberhorn, and U. Peschel, *Phys. Rev. Lett.* **107**, 233902 (2011).
- [52] M. Wimmer, M.-A. Miri, D. Christodoulides, and U. Peschel, *Scientific Reports* **5**, 17760 (2015).
- [53] J. K. Asbóth and H. Obuse, *Phys. Rev. B* **88**, 121406 (2013).
- [54] A. Bisianov, A. Muniz, U. Peschel, and O. A. Egorov, *Phys. Rev. A* **102**, 053511 (2020).
- [55] C. Cedzich, T. Geib, F. A. Grünbaum, C. Stahl, L. Velázquez, A. H. Werner, and R. F. Werner, *Annales Henri Poincaré* **19**, 325 (2018).
- [56] T. Kitagawa, M. S. Rudner, E. Berg, and E. Demler, *Phys. Rev. A* **82**, 033429 (2010).
- [57] T. Kitagawa, M. A. Broome, A. Fedrizzi, M. S. Rudner, E. Berg, I. Kassal, A. Aspuru-Guzik, E. Demler, and A. G. White, *Nature Communications* **3**, 882 (2012).
- [58] T. Nitsche, T. Geib, C. Stahl, L. Lorz, C. Cedzich, S. Barkhofen, R. F. Werner, and C. Silberhorn, *New Journal of Physics* **21**, 043031 (2019).
- [59] M. Wimmer, H. M. Price, I. Carusotto, and U. Peschel, *Nature Physics* **13**, 545 (2017).
- [60] S. E. Venegas-Andraca, *Quantum Information Processing* **11**, 1015 (2012).
- [61] E. Farhi and S. Gutmann, *Phys. Rev. A* **58**, 915 (1998).
- [62] Y. Aharonov, L. Davidovich, and N. Zagury, *Phys. Rev. A* **48**, 1687 (1993).
- [63] P. A. M. Dirac, K. Gupta, and G. Sudershan, *Lectures on Quantum Mechanics and Relativistic Field Theory* (Tata Institute of Fundamental Research, 1955).
- [64] M. Holthaus, *Journal of Physics B: Atomic, Molecular and Optical Physics* **49**, 013001 (2015).
- [65] M.-A. Miri, A. Regensburger, U. Peschel, and D. N. Christodoulides, *Phys. Rev. A* **86**, 023807 (2012).

- [66] N. W. Ashcroft, N. D. Mermin, *et al.*, “Solid state physics,” (1976).
- [67] S. Ryu, A. P. Schnyder, A. Furusaki, and A. W. W. Ludwig, *New Journal of Physics* **12**, 065010 (2010).
- [68] T. Kitagawa, E. Berg, M. Rudner, and E. Demler, *Phys. Rev. B* **82**, 235114 (2010).
- [69] M. S. Rudner, N. H. Lindner, E. Berg, and M. Levin, *Phys. Rev. X* **3**, 031005 (2013).
- [70] L. J. Maczewsky, J. M. Zeuner, S. Nolte, and A. Szameit, *Nature Communications* **8**, 13756 (2017).
- [71] F. D. M. Haldane, *Phys. Rev. Lett.* **61**, 2015 (1988).
- [72] R. B. Laughlin, *Phys. Rev. Lett.* **50**, 1395 (1983).
- [73] K. Esaki, M. Sato, K. Hasebe, and M. Kohmoto, *Phys. Rev. B* **84**, 205128 (2011).
- [74] L. Fu and C. L. Kane, *Phys. Rev. B* **74**, 195312 (2006).
- [75] J. Zak, *Phys. Rev. Lett.* **62**, 2747 (1989).
- [76] C. L. Kane and E. J. Mele, *Phys. Rev. Lett.* **95**, 146802 (2005).
- [77] M. V. Berry, *Proceedings of the Royal Society of London. A. Mathematical and Physical Sciences* **392**, 45 (1984).
- [78] A. P. Schnyder, S. Ryu, A. Furusaki, and A. W. W. Ludwig, *Phys. Rev. B* **78**, 195125 (2008).
- [79] C. Cedzich, F. A. Grünbaum, C. Stahl, L. Velázquez, A. H. Werner, and R. F. Werner, *Journal of Physics A: Mathematical and Theoretical* **49**, 21LT01 (2016).
- [80] W. P. Su, J. R. Schrieffer, and A. J. Heeger, *Phys. Rev. Lett.* **42**, 1698 (1979).
- [81] A. Bisianov, M. Wimmer, U. Peschel, and O. A. Egorov, *Phys. Rev. A* **100**, 063830 (2019).
- [82] M. Kremer, *Topological Effects in Fibre Networks*, Master’s thesis, Friedrich-Schiller-Universität Jena (2017).
- [83] J. Du, H. Li, X. Xu, M. Shi, J. Wu, X. Zhou, and R. Han, *Phys. Rev. A* **67**, 042316 (2003).
- [84] C. A. Ryan, M. Laforest, J. C. Boileau, and R. Laflamme, *Phys. Rev. A* **72**, 062317 (2005).
- [85] F. Zähringer, G. Kirchmair, R. Gerritsma, E. Solano, R. Blatt, and C. F. Roos, *Phys. Rev. Lett.* **104**, 100503 (2010).
- [86] H. Schmitz, R. Matjeschk, C. Schneider, J. Glueckert, M. Enderlein, T. Huber, and T. Schaetz, *Phys. Rev. Lett.* **103**, 090504 (2009).
- [87] M. Karski, L. Förster, J.-M. Choi, A. Steffen, W. Alt, D. Meschede, and A. Widera, *Science* **325**, 174 (2009).
- [88] M. Genske, W. Alt, A. Steffen, A. H. Werner, R. F. Werner, D. Meschede, and A. Alberti, *Phys. Rev. Lett.* **110**, 190601 (2013).

- [89] K. Poullos, R. Keil, D. Fry, J. D. A. Meinecke, J. C. F. Matthews, A. Politi, M. Lobino, M. Gräfe, M. Heinrich, S. Nolte, A. Szameit, and J. L. O'Brien, *Phys. Rev. Lett.* **112**, 143604 (2014).
- [90] L. Sansoni, F. Sciarrino, G. Vallone, P. Mataloni, A. Crespi, R. Ramponi, and R. Osellame, *Phys. Rev. Lett.* **108**, 010502 (2012).
- [91] M. A. Broome, A. Fedrizzi, B. P. Lanyon, I. Kassal, A. Aspuru-Guzik, and A. G. White, *Phys. Rev. Lett.* **104**, 153602 (2010).
- [92] H. B. Perets, Y. Lahini, F. Pozzi, M. Sorel, R. Morandotti, and Y. Silberberg, *Phys. Rev. Lett.* **100**, 170506 (2008).
- [93] A. Peruzzo, M. Lobino, J. C. F. Matthews, N. Matsuda, A. Politi, K. Poullos, X.-Q. Zhou, Y. Lahini, N. Ismail, K. Wörhoff, Y. Bromberg, Y. Silberberg, M. G. Thompson, and J. L. OBrien, *Science* **329**, 1500 (2010).
- [94] A. Schreiber, K. N. Cassemiro, V. Potocek, A. Gábris, P. J. Mosley, E. Andersson, I. Jex, and C. Silberhorn, *Phys. Rev. Lett.* **104**, 050502 (2010).
- [95] M. Wimmer, A. Regensburger, C. Bersch, M.-A. Miri, S. Batz, G. Onishchukov, D. N. Christodoulides, and U. Peschel, *Nature Physics* **9**, 780 (2013).
- [96] A. Schreiber, *Quantum Walks in Time*, Ph.D. thesis, Friedrich-Alexander-Universitaet Erlangen-Nuernberg (2013).
- [97] F. Bloch, *Zeitschrift für Physik* **52**, 555 (1929).
- [98] P. W. Anderson, *Phys. Rev.* **109**, 1492 (1958).
- [99] J. I. Pascual, J. Méndez, J. Gómez-Herrero, A. M. Baró, N. Garcia, U. Landman, W. D. Luedtke, E. N. Bogachek, and H. P. Cheng, *Science* **267**, 1793 (1995).
- [100] T. Ying, Y. Gu, X. Chen, X. Wang, S. Jin, L. Zhao, W. Zhang, and X. Chen, *Science Advances* **2**, e1501283 (2016).
- [101] M. Segev, Y. Silberberg, and D. N. Christodoulides, *Nature Photonics* **7**, 197 (2013).
- [102] D. S. Wiersma, *Nature Photonics* **7**, 188 (2013).
- [103] T. Schwartz, G. Bartal, S. Fishman, and M. Segev, *Nature* **446**, 52 (2007).
- [104] J. Billy, V. Josse, Z. Zuo, A. Bernard, B. Hambrecht, P. Lugan, D. Clément, L. Sanchez-Palencia, P. Bouyer, and A. Aspect, *Nature* **453**, 891 (2008).
- [105] G. Roati, C. D'Errico, L. Fallani, M. Fattori, C. Fort, M. Zaccanti, G. Modugno, M. Modugno, and M. Inguscio, *Nature* **453**, 895 (2008).
- [106] H. Hu, A. Strybulevych, J. H. Page, S. E. Skipetrov, and B. A. van Tiggelen, *Nature Physics* **4**, 945 (2008).
- [107] A. Lagendijk, B. v. Tiggelen, and D. S. Wiersma, *Physics Today* **62**, 24 (2009).
- [108] E. Abrahams, *50 years of Anderson Localization*, Vol. 24 (world scientific, 2010).

- [109] S. Datta, *Electronic Transport in Mesoscopic Systems*, Cambridge Studies in Semiconductor Physics and Microelectronic Engineering (Cambridge University Press, 1995).
- [110] L. Sapienza, H. Thyrrerstrup, S. Stobbe, P. D. Garcia, S. Smolka, and P. Lodahl, *Science* **327**, 1352 (2010).
- [111] J. Liu, P. D. Garcia, S. Ek, N. Gregersen, T. Suhr, M. Schubert, J. Mørk, S. Stobbe, and P. Lodahl, *Nature Nanotechnology* **9**, 285 (2014).
- [112] D. S. Wiersma, *Nature Physics* **4**, 359 (2008).
- [113] P. Stano and P. Jacquod, *Nature Photonics* **7**, 66 (2013).
- [114] J. Li, R.-L. Chu, J. K. Jain, and S.-Q. Shen, *Phys. Rev. Lett.* **102**, 136806 (2009).
- [115] E. J. Meier, F. A. An, A. Dauphin, M. Maffei, P. Massignan, T. L. Hughes, and B. Gadway, *Science* **362**, 929 (2018).
- [116] S. Stützer, Y. Plotnik, Y. Lumer, P. Titum, N. H. Lindner, M. Segev, M. C. Rechtsman, and A. Szameit, *Nature* **560**, 461 (2018).
- [117] I. Vakulchyk, M. V. Fistul, P. Qin, and S. Flach, *Phys. Rev. B* **96**, 144204 (2017).
- [118] S. Derevyanko, *Scientific Reports* **8**, 1795 (2018).
- [119] A. V. Pankov, I. D. Vatnik, D. V. Churkin, and S. A. Derevyanko, *Opt. Express* **27**, 4424 (2019).
- [120] A. Schreiber, K. N. Cassemiro, V. Potoček, A. Gábris, I. Jex, and C. Silberhorn, *Phys. Rev. Lett.* **106**, 180403 (2011).
- [121] I. D. Vatnik, A. Tikan, G. Onishchukov, D. V. Churkin, and A. A. Sukhorukov, *Scientific Reports* **7**, 4301 (2017).
- [122] G. Stolz, *Entropy and the quantum II. Contemp. Math* **552**, 71 (2011).
- [123] V. Bucaj, D. Damanik, J. Fillman, V. Gerbuz, T. VandenBoom, F. Wang, and Z. Zhang, *Transactions of the American Mathematical Society* **372**, 3619 (2019).
- [124] B. Kramer and A. MacKinnon, *Reports on Progress in Physics* **56**, 1469 (1993).
- [125] F. Germinet and A. Taarabt, *Reviews in Mathematical Physics* **25**, 1350016 (2013).
- [126] R. del Rio, S. Jitomirskaya, Y. Last, and B. Simon, *Phys. Rev. Lett.* **75**, 117 (1995).
- [127] P. Phillips and H.-L. Wu, *Science* **252**, 1805 (1991).
- [128] N. F. Mott, *The Philosophical Magazine: A Journal of Theoretical Experimental and Applied Physics* **19**, 835 (1969).
- [129] N. F. Mott and E. A. Davis, *Electronic processes in non-crystalline materials* (Oxford university press, 2012).
- [130] T. V. Lapyeva, A. A. Tikhomirov, O. I. Kanakov, and M. V. Ivanchenko, *Scientific Reports* **5**, 13263 (2015).

-
- [131] A. Basiri, Y. Bromberg, A. Yamilov, H. Cao, and T. Kottos, *Phys. Rev. A* **90**, 043815 (2014).
- [132] N. Hatano and D. R. Nelson, *Phys. Rev. Lett.* **77**, 570 (1996).
- [133] N. Hatano and D. R. Nelson, *Phys. Rev. B* **58**, 8384 (1998).
- [134] I. I. Yusipov, T. V. Lapyeva, and M. V. Ivanchenko, *Phys. Rev. B* **97**, 020301 (2018).
- [135] A. F. Tzortzakakis, K. G. Makris, and E. N. Economou, *Phys. Rev. B* **101**, 014202 (2020).
- [136] Y. Huang and B. I. Shklovskii, *Phys. Rev. B* **101**, 014204 (2020).
- [137] A. G. Yamilov, R. Sarma, B. Redding, B. Payne, H. Noh, and H. Cao, *Phys. Rev. Lett.* **112**, 023904 (2014).
- [138] I. Yusipov, T. Lapyeva, S. Denisov, and M. Ivanchenko, *Phys. Rev. Lett.* **118**, 070402 (2017).
- [139] R. Hamazaki, K. Kawabata, and M. Ueda, *Phys. Rev. Lett.* **123**, 090603 (2019).
- [140] M. Balasubrahmaniam, S. Mondal, and S. Mujumdar, *Phys. Rev. Lett.* **124**, 123901 (2020).
- [141] B. A. van Tiggelen, A. Lagendijk, and D. S. Wiersma, *Phys. Rev. Lett.* **84**, 4333 (2000).
- [142] J. Wang and A. Z. Genack, *Nature* **471**, 345 (2011).
- [143] C.-S. Tian, S.-K. Cheung, and Z.-Q. Zhang, *Phys. Rev. Lett.* **105**, 263905 (2010).
- [144] J. B. Pendry, *Journal of Physics C: Solid State Physics* **20**, 733 (1987).
- [145] J. Bertolotti, S. Gottardo, D. S. Wiersma, M. Ghulinyan, and L. Pavesi, *Phys. Rev. Lett.* **94**, 113903 (2005).
- [146] I. V. Barashenkov, D. A. Zezyulin, and V. V. Konotop, *New Journal of Physics* **18**, 075015 (2016).
- [147] S. A. R. Horsley and S. Longhi, *American Journal of Physics* **85**, 439 (2017).
- [148] F. Klauck, L. Teuber, M. Ornigotti, M. Heinrich, S. Scheel, and A. Szameit, *Nature Photonics* **13**, 883 (2019).
- [149] T. Eichelkraut, R. Heilmann, S. Weimann, S. Stützer, F. Dreisow, D. N. Christodoulides, S. Nolte, and A. Szameit, *Nature Communications* **4**, 2533 (2013).
- [150] L. Teuber and S. Scheel, *Phys. Rev. A* **101**, 042124 (2020).
- [151] S. Scheel and A. Szameit, *EPL* **124** (2018).
- [152] X. Luo, T. Ohtsuki, and R. Shindou, *Phys. Rev. Lett.* **126**, 090402 (2021).
- [153] Y. Xiong, *Journal of Physics Communications* **2**, 035043 (2018).
- [154] A. Ghatak and T. Das, *Journal of Physics: Condensed Matter* **31**, 263001 (2019).

- [155] C. H. Lee and R. Thomale, Phys. Rev. B **99**, 201103 (2019).
- [156] V. M. Martinez Alvarez, J. E. Barrios Vargas, and L. E. F. Foa Torres, Phys. Rev. B **97**, 121401 (2018).
- [157] T. E. Lee, Phys. Rev. Lett. **116**, 133903 (2016).
- [158] F. K. Kunst, E. Edvardsson, J. C. Budich, and E. J. Bergholtz, Phys. Rev. Lett. **121**, 026808 (2018).
- [159] N. Okuma, K. Kawabata, K. Shiozaki, and M. Sato, Phys. Rev. Lett. **124**, 086801 (2020).
- [160] R. Koch and J. C. Budich, The European Physical Journal D **74**, 70 (2020).
- [161] E. J. Bergholtz, J. C. Budich, and F. K. Kunst, Rev. Mod. Phys. **93**, 015005 (2021).
- [162] H. Shen, B. Zhen, and L. Fu, Phys. Rev. Lett. **120**, 146402 (2018).
- [163] C. Poli, M. Bellec, U. Kuhl, F. Mortessagne, and H. Schomerus, Nature Communications **6**, 6710 (2015).
- [164] M. Kremer, T. Biesenthal, L. J. Maczewsky, M. Heinrich, R. Thomale, and A. Szameit, Nature Communications **10**, 435 (2019).
- [165] A. Mostafazadeh, Journal of Mathematical Physics **43**, 205 (2002).
- [166] A. Regensburger, *Experiments on pulse dynamics and parity-time symmetry in optical fiber networks*, Ph.D. thesis, Friedrich-Alexander-Universitaet Erlangen-Nuernberg (2013).
- [167] L. Xiao, T. Deng, K. Wang, G. Zhu, Z. Wang, W. Yi, and P. Xue, Nature Physics **16**, 761 (2020).
- [168] T. Helbig, T. Hofmann, S. Imhof, M. Abdelghany, T. Kiessling, L. W. Molenkamp, C. H. Lee, A. Szameit, M. Greiter, and R. Thomale, Nature Physics **16**, 747 (2020).
- [169] J. C. Budich and E. J. Bergholtz, Phys. Rev. Lett. **125**, 180403 (2020).
- [170] S. Longhi, Opt. Lett. **47**, 2040 (2022).
- [171] S. Longhi, Phys. Rev. Lett. **128**, 157601 (2022).
- [172] C. M. Bender, M. V. Berry, and A. Mandilara, Journal of Physics A: Mathematical and General **35**, L467 (2002).
- [173] K. G. Makris, R. El-Ganainy, D. N. Christodoulides, and Z. H. Musslimani, Phys. Rev. Lett. **100**, 103904 (2008).
- [174] Y. C. Hu and T. L. Hughes, Phys. Rev. B **84**, 153101 (2011).
- [175] Y. E. Kraus and O. Zilberberg, Nature Physics **12**, 624 (2016).
- [176] D. Shechtman, I. Blech, D. Gratias, and J. W. Cahn, Phys. Rev. Lett. **53**, 1951 (1984).
- [177] S. Aubry and G. André, Ann. Israel Phys. Soc **3**, 18 (1980).

-
- [178] P. G. Harper, Proceedings of the Physical Society. Section A **68**, 874 (1955).
- [179] D. R. Hofstadter, Phys. Rev. B **14**, 2239 (1976).
- [180] Y. Lahini, R. Pugatch, F. Pozzi, M. Sorel, R. Morandotti, N. Davidson, and Y. Silberberg, Phys. Rev. Lett. **103**, 013901 (2009).
- [181] M. Verbin, O. Zilberberg, Y. E. Kraus, Y. Lahini, and Y. Silberberg, Phys. Rev. Lett. **110**, 076403 (2013).
- [182] O. Zilberberg, Opt. Mater. Express **11**, 1143 (2021).
- [183] H. Jiang, L.-J. Lang, C. Yang, S.-L. Zhu, and S. Chen, Phys. Rev. B **100**, 054301 (2019).
- [184] S. Longhi, Phys. Rev. B **100**, 125157 (2019).
- [185] Q.-B. Zeng, Y.-B. Yang, and Y. Xu, Phys. Rev. B **101**, 020201 (2020).
- [186] S. Longhi, Phys. Rev. Lett. **122**, 237601 (2019).
- [187] Y. Liu, Q. Zhou, and S. Chen, Phys. Rev. B **104**, 024201 (2021).
- [188] T. Liu, H. Guo, Y. Pu, and S. Longhi, Phys. Rev. B **102**, 024205 (2020).
- [189] Q.-B. Zeng and Y. Xu, Phys. Rev. Research **2**, 033052 (2020).
- [190] J. Sokoloff, Physics Reports **126**, 189 (1985).
- [191] S. Longhi, Phys. Rev. Research **1**, 023013 (2019).
- [192] Q. Lin, T. Li, L. Xiao, K. Wang, W. Yi, and P. Xue, arXiv , 2112.15024 (2021).
- [193] S. Longhi, Opt. Lett. **44**, 1190 (2019).
- [194] C. Cedzich, J. Fillman, T. Geib, and A. H. Werner, Letters in Mathematical Physics **110**, 1141 (2020).
- [195] A. Schreiber, A. Gábris, P. P. Rohde, K. Laiho, M. Štefaňák, V. Potoček, C. Hamilton, I. Jex, and C. Silberhorn, Science **336**, 55 (2012).
- [196] A. L. M. Muniz, M. Wimmer, A. Bisianov, U. Peschel, R. Morandotti, P. S. Jung, and D. N. Christodoulides, Phys. Rev. Lett. **123**, 253903 (2019).
- [197] M. Wimmer, A. Regensburger, M.-A. Miri, C. Bersch, D. N. Christodoulides, and U. Peschel, Nature Communications **6**, 7782 (2015).

Conference contributions

Talks

- **Non-Hermitian quantum walks in coupled optical fibre loops**
Week of the Young Researcher, Quantum Science: Light Matter Interaction
2019, Moscow, Russia
- **Topological effects in optical fibre loop systems**
From Topology to Photonics and beyond (Alfried Krupp Wissenschaftskolleg)
2019, Greifswald, Germany
- **Observation of Non-Hermitian Anderson Transport**
Conference on Lasers and Electro-Optics (CLEO)
2020, San Jose, USA (Virtual conference)
Awarded Finalist of the Maiman Student Paper Competition
- **Observation of Non-Hermitian Anderson Transport**
Deutsche Physikalische Gesellschaft – spring meeting
2020, Hannover, Germany
Conference cancelled, abstract and talk accepted
- **Building a Light Funnel with the non-Hermitian Skin Effect**
Deutsche Physikalische Gesellschaft – spring meeting
2020, Hannover, Germany
Conference cancelled, abstract and talk accepted
- **Non-Hermitian phase transition induced by fractal potentials**
Conference on Lasers and Electro-Optics (CLEO)
2021, San Jose, USA (Virtual conference)
- **Implementation of a non-Hermitian phase transition in quasicrystals based on a Floquet Aubry-André-Harper model**
Conference on Lasers and Electro-Optics Europe (CLEO EU)
2021, Munich, Germany (Virtual conference)
- **Floquet Hofstadter Butterflies and a Topological Triple Phase Transition in Quasicrystals**
8th International Symposium: Optics & its Applications (OPTICA)
2021, Rostock, Germany
Awarded best student talk
- **Topological triple phase transition in non-Hermitian Floquet quasicrystals**
Workshop: Modern Concepts of Topological and Quantum Photonics
2022, Rostock, Germany

Posters

- **Non-Hermitian quantum walks in coupled optical fibre loops**
Week of the Young Researcher, Quantum Science: Light Matter Interaction
2019, Moscow, Russia